

INFORMATION TO USERS

The most advanced technology has been used to photograph and reproduce this manuscript from the microfilm master. UMI films the original text directly from the copy submitted. Thus, some dissertation copies are in typewriter face, while others may be from a computer printer.

In the unlikely event that the author did not send UMI a complete manuscript and there are missing pages, these will be noted. Also, if unauthorized copyrighted material had to be removed, a note will indicate the deletion.

Oversize materials (e.g., maps, drawings, charts) are reproduced by sectioning the original, beginning at the upper left-hand corner and continuing from left to right in equal sections with small overlaps. Each oversize page is available as one exposure on a standard 35 mm slide or as a 17" × 23" black and white photographic print for an additional charge.

Photographs included in the original manuscript have been reproduced xerographically in this copy. 35 mm slides or 6" × 9" black and white photographic prints are available for any photographs or illustrations appearing in this copy for an additional charge. Contact UMI directly to order.



300 North Zeeb Road, Ann Arbor, MI 48106-1346 USA

Order Number 8729424

The evolution of cometary activity

Storrs, Alexander David, Ph.D.

University of Hawaii, 1987

U·M·I
300 N. Zeeb Rd.
Ann Arbor, MI 48106

PLEASE NOTE:

In all cases this material has been filmed in the best possible way from the available copy. Problems encountered with this document have been identified here with a check mark ✓.

1. Glossy photographs or pages _____
2. Colored illustrations, paper or print _____
3. Photographs with dark background ✓
4. Illustrations are poor copy _____
5. Pages with black marks, not original copy _____
6. Print shows through as there is text on both sides of page _____
7. Indistinct, broken or small print on several pages ✓
8. Print exceeds margin requirements _____
9. Tightly bound copy with print lost in spine _____
10. Computer printout pages with indistinct print _____
11. Page(s) _____ lacking when material received, and not available from school or author.
12. Page(s) _____ seem to be missing in numbering only as text follows.
13. Two pages numbered _____. Text follows.
14. Curling and wrinkled pages _____
15. Dissertation contains pages with print at a slant, filmed as received _____
16. Other _____

University
Microfilms
International

THE EVOLUTION OF COMETARY ACTIVITY

**A DISSERTATION SUBMITTED TO THE GRADUATE DIVISION OF THE
UNIVERSITY OF HAWAII IN PARTIAL FULFILLMENT
OF THE REQUIREMENTS FOR THE DEGREE OF**

**DOCTOR OF PHILOSOPHY
IN ASTRONOMY**

AUGUST 1987

By

Alexander David Storrs

Dissertation Committee:

**Dale P. Cruikshank, Chairman
Fraser P. Fanale
Jonathan C. Gradie
Alan N. Stockton
Chester A. Vause**

ACKNOWLEDGEMENTS

This work was supported by NASA Graduate Student Research Fellowship NGT-12-004-800. Additional support from NASA Grants NGL-12-001-454 and NGL-12-001-057 is gratefully acknowledged.

The simulations would have been impossible without the assistance and advice of Eric Laue of JPL. The SEM work was capably performed by Ronald P. Ruiz and Russell A. Lawton. Marcia Nelson, Eileen Bruckenthal, and Larry Lebofsky gave invaluable discussions of possible interpretations of the FSR formation process. James Stephens, Dennis Matson, Moustafa Chahine, and Harold Ashkenaz provided valuable on lab support and advice.

The Mauna Kea support staff, particularly telescope operators Bruce Barnes and Frank Cheigh, were instrumental in allowing the observations to be made. Robert Hlivak and J. Patrick Henry were very helpful in determining the flat-field problems. Michael A'Hearn and David Schleicher gave many helpful discussions at all stages of the project. Simon Lilly was very kind in allowing me to use a few hours of his 88" time to make the April observations.

My committee, and particularly Dale Cruikshank and Fraser Fanale, were essential to the successful completion of this work. I cannot say enough to thank these gentlemen for their assistance.

Finally, I would like to thank my mother, who reminded me that, whatever the job situation, "there's always room at the top for the best".

ABSTRACT

This dissertation is a two part investigation into the manner in which cometary activity originates. The first part is a simulation of the formation of a refractory residue layer on a surface subliming dirty ice. The second part traces to morphology of the sublimed ice (now gas) as it flows out through the inner coma.

The formation of filamentary sublimate (FSR) residues from subliming dirty ice has been discussed by Saunders et al, (1984). The first part of this dissertation expands on the study of Saunders et al, by testing all major silicate mineral classes, and investigating the effects of organic materials on the formation of these residues. FSR is a light, strong material, an excellent thermal insulator, and its presence on the surface of cometary nuclei (and, potentially, on Martian polar layered terrain and icy satellites) would strongly affect the evolution of gas from the volatile ices it covers.

FSR is formed when hydrated phyllosilicate grains are released from an icy matrix. These mineral grains attract a coating of several monolayers of semifluid water around themselves, even though the surrounding water is frozen. This semifluid layer allows the grains to coordinate and rebond into larger units. These units are chemically identical to the original material, while retaining the physical morphology of the dirty ice. Organic tars can also bind mineral grains together. The structure formed is stronger and less porous than pure mineral FSR. Organic FSR resembles the structure observed to cover most of the nucleus of Halley's comet (Keller et al. 1986).

The second part of this dissertation investigates the morphology of the outflow of the OH radical in the inner coma of Halley's comet. When a ratio is made of images of the comet in the OH (1-1) and (0-0) bands (around 3100 Å), the resulting image maps the projection along the line of sight of the sunward velocity of the gas in the coma. Qualitative interpretation of these images shows that, although constant velocity, spherically symmetric outflow is usually observed, gas jets and other asymmetries are not uncommon. Poor quantitative agreement with the theory (Schleicher and A'Hearn 1982) suggests either gas outflows on the order of 4 km/sec, or fine structure in the ratio which was not modeled by Schleicher and A'Hearn.

TABLE OF CONTENTS

ACKNOWLEDGEMENTS	iii
ABSTRACT	iv
LIST OF TABLES	vii
LIST OF FIGURES	viii
CHAPTER 1--INTRODUCTION	1
CHAPTER 2--FILAMENTARY SUBLIMATE RESIDUE	9
Method	9
Results	12
Analysis	22
Other Results	26
Organics	28
Discussion	33
CHAPTER 3--GREENSTEIN EFFECT	39
Modeling	39
Observations	41
Image Reduction	41
OH1 Excess	43
Results	46
Conclusions	58
CHAPTER 4--SUMMARY	60
APPENDIX--OBSERVATIONAL PROCEDURES	63
Image Acquisition	64
Basic Image Reduction	64

Flat Fielding	67
Extinction Correction	69
Sensitivity Correction	77
Cosmetic Processing	77
Continuum Correction	78
Summary	80
BIBLIOGRAPHY	81

LIST OF TABLES

1. Major Mineral Groups	13
2. Phyllosilicates	14
3. Properties of FSR	34
4. OH Observations	42
5. Extinction Factors	74

LIST OF FIGURES

1. OH Band Intensities and Ratios	6
2. Calculated Ratio Map	7
3. Simulations Apparatus	10
4. FSR in Dewar	15
5. Montmorillonite--Raw and FSR	17
6. Cab-o-sil FSR	21
7. Silicate Mineral Structure	23
8. Botrioidal FSR	24
9. Spectrum of Organic Material	31
10. Organic FSR	32
11. Image Profiles	44
12. OH1 Excess Image	45
13. OH Ratio Images	47
14. Error Images	57
15. Filter Profiles	65
16. Flat Field Observational Geometry	68
17. Flat Fields and Correction Surface	70
18. Extinction Curves	72

CHAPTER 1

Introduction

The solar system probably formed from a collapsing cloud of gas and dust. Regardless of how the initial collapse was triggered (by outflows from other forming stars or by gas and dust thrown off by planetary nebulae or supernovae), conservation of angular momentum requires that the cloud quickly assume an oblate, disk-like shape. This disk is commonly referred to as the protosolar nebula (PSN).

Theoretical studies (cf. Goldreich and Ward 1973) show that refractory grains in the PSN would settle to the midplane of the disk due to gas drag. Theory further predicts that the thin, massive dust disk formed at the center of the thicker, gassy disk would develop gravitational instabilities, and collapse further into bodies of about 1 km in size. Although these "planetesimals" would initially be in circular, prograde orbits, they would eventually start to interact with each other and combine to form larger bodies. The investigation of Greenberg et al (1984) showed how an initially uniform annulus of 1-10 km sized planetesimals could evolve into one large planet, with the few left-over planetesimals perturbed into orbits that do not encounter the protoplanet. Their dynamical calculations have shown that planetesimals that are not accreted into Jupiter and Saturn acquire enough energy during close encounters with these bodies in their protoplanetary stage to be removed from the solar system entirely, on hyperbolic orbits. Planetesimals that were not accreted into Uranus or Neptune would, in general, be perturbed onto highly elongated, but still bound, orbits. These orbits are very much like those on which long-period comets are found today. What we see as comets are generally thought to be remnant planetesimals, the left-over building blocks of the outer planets.

Models of the chemistry of the PSN usually assume that all materials were vaporized upon accretion into the PSN. (That this happened is by no means clear. Indeed, in a popular theory for the composition of comets (Greenberg, 1982) the grains consist of agglomerations of more or less unaltered interstellar material.) The equilibrium condensation hypothesis of the chemical makeup of planetesimals

(Barshay and Lewis 1976) holds that solid bodies condensing in the PSN retain the chemical makeup of the temperature of the PSN at the time and distance at which they condensed. If all the materials in the PSN were vaporized, the refractory compounds would start to recondense very quickly in the outer, cooler regions. Thus, bodies formed near the sun should mainly consist of high-temperature condensates (predominantly silicate minerals and metal), while those forming farther out in the PSN would retain significant amounts of water ice, and those even farther out, methane and ammonia and more volatile compounds. Knowledge of the chemical makeup of comets would greatly aid our understanding of the condensation conditions of the outer PSN (assuming, of course, that this theory of cometary formation is correct).

The composition of a planetesimal is not likely to remain constant as it is perturbed into a cometary orbit. The perturbation process is believed to involve several encounters between the planetesimal and the growing protoplanet. Conditions near the protoplanet are likely to have been very different from those of the PSN where the planetesimal initially formed. A planetesimal may be perturbed into regions of the PSN much warmer than those in which it formed, causing depletion of some of its most volatile compounds. The planetesimal might also be perturbed into regions much colder than those in which it formed, where it may accrete even more volatile compounds.

Long period ("new") comets are observed to have orbits whose aphelia are at about 10^4 AU from the sun, and randomly distributed in direction. These observations describe a "shell" of comets around the solar system. This shell is commonly called the "Oort cloud", after Jan Oort, who first proposed this interpretation. Comets on these long-period orbits can survive, with little alteration for the lifetime of the solar system.

"Storage" in the Oort cloud is not an entirely benign process. Johnson et al. (1987) discuss the depletion of volatiles in the outer few meters of a planetesimal on a cometary orbit, by bombardment with galactic cosmic rays. Over long periods, this bombardment tends to deplete the surface of the comet of volatile elements, leaving the heavier ones to combine into even more refractory molecules. Johnson et al suggest that this process would lead to the formation of compounds not found in the PSN.

The major change in composition of comets occurs when they pass close to the sun. The sublimation of (primarily) water ice will carry the smaller refractory grains away from the nucleus, but should leave behind the largest grains. If there is any cohesion among the grains, a volatile-poor mantle could quickly form on the surface of the comet's nucleus, limiting the outgassing of water. The structure of such a mantle, and its ability to inhibit sublimation, are investigated in the second chapter of this dissertation.

Sublimation of impure ("dirty") water ice is not uncommon in the inner solar system. In addition to its importance as the source of cometary activity, it is believed to be important in the formation of polar layered terrain on Mars (Pollack and Toon, 1982, and references therein). Sublimation must occur to some extent on the surfaces of icy satellites, although impact of the solar wind and planetary magnetospheric ions probably has a much greater effect (R. Johnson, pvt. comm.).

When removal of ices is slow enough, the refractory impurities are left behind on the surface of the body. Such lag deposits may be seen in the Martian layered terrain, where the striations observed are interpreted as variations in the dust content of an otherwise fairly uniform icy cap (Cutts and Lewis, 1982). Lag deposits (mantles) have also been inferred to be a common occurrence on the surfaces of cometary nuclei. This inference is in part due to reduced activity of "older comets" and in part due to the observation of "jets" of dust near cometary nuclei. The presence of such a mantle received dramatic confirmation during the Giotto flyby of Halley's comet in March, 1986, when the first pictures of a comet's nucleus were sent back to the Earth. These showed the nucleus to be a large, dark object, emitting dust primarily from specific points on its surface (Keller et al., 1986, Reitsema et al., 1987). The observation of limited outflow from the nucleus requires that most of its surface be covered by a dark, volatile-poor substance.

Laboratory simulations of martian conditions exhibited some unforeseen behavior. When populations of small dust particles were allowed to equilibrate with volatile atmospheres (e.g. water, Johnson et al 1975, and CO₂, Greeley 1979) and then exposed to markedly lower pressures, dust fountains and jets were observed to form, implying some cohesion in the surface layer of dust. Saunders et al. (1986)

observed formation of a "fluffy filamentary sublimate residue material" during experiments simulating martian polar and cometary conditions. Only Saunders et al. investigated this process any further and, beyond the suggestion of vacuum welding of extremely clean grains, they did not shed more light on the grain-binding process.

The second chapter of this dissertation reports the results of a series of experiments designed to determine the generality of this grain-binding process, and to better characterize where it might occur in the solar system. All the major groups of silicate minerals were tested in a manner similar to that used by Saunders et al. The effect of organic (tarry) material on grain binding was also investigated, in an attempt to simulate what is believed to be the cometary environment.

The most direct method for determining the composition of a comet from the Earth is to make spectroscopic measurements of the molecules in its head (coma). The molecules most frequently observed are not those found in the nucleus (the "parent molecules"), but are derived from the breakdown of the parent molecules. They are thus referred to as "daughter molecules". Parent molecules are usually quite fragile, and break down rapidly under the intense ultraviolet flux from the sun. Scanning a spectrum radially away from the nucleus (along an emission line), the brightness of the line would increase sharply near the nucleus (due to production of the emitting daughter molecules by breakdown of the parent molecules), and decay (generally, somewhat more slowly) due to the dispersion and further breakdown or de-excitation of the daughter molecules.

Inversion of the observed surface brightness distribution of the coma to get the spatial density of the daughter molecules requires knowledge of how the gas flows in the inner coma. This flow is usually assumed to be spherically symmetric about the nucleus. The parent molecules are released radially outward, at the velocity corresponding to their temperature of sublimation. The daughter molecules either maintain this velocity (the Haser model, Haser 1957, described in Krishna Swamy 1986, pp. 104-108), or obey equipartition of energy in the breakdown of the parent, with this additional velocity randomly oriented with respect to the initial outflow direction (the vectorial model, Festou 1981).

Greenstein (1958) reported that, in comet Mrkos, line strengths in the 3800 Å band of the CN radical varied between the sunward and antisunward side of the optocenter. He interpreted this variation by examining the solar spectrum in the region around 3800 Å. Most radicals in the inner coma of comets are observed to be excited entirely by resonance fluorescence with the incident sunlight. In the ultraviolet (UV) region, the sun's spectrum is broken by many strong, sharp absorption lines. Greenstein noted that, as cometary gas flows towards the sun from the nucleus, it is excited by a solar spectrum that is slightly blueshifted with respect to the spectrum exciting the gas flowing away from the sun and the nucleus. The presence of an absorption line in the solar spectrum would result in a marked change in exciting flux for a small change in sunward velocity. This change in exciting flux explained the sunward-antisunward variation in the CN lines he had observed.

Schleicher and A'Hearn (1982) reported the results of theoretical calculations of the Greenstein effect for the OH radical. Their calculations showed that the intensity of the OH (0-0), (1-1), and (1-0) bands of the $A^2\Sigma^+ - X^2\Pi$ transition should vary markedly with the heliocentric velocity of the gas. The (0-0) and (1-1) bands have band heads at 3064 Å and 3122 Å respectively, and are therefore barely observable from the ground. Schleicher and A'Hearn pointed out that the ratio of the fluxes in these bands should be independent of the gas density (in radiative equilibrium), and depend only on the heliocentric velocity of the emitting gas. Figure 1 shows the variation of the intensity of these bands, and of the band ratios, with heliocentric velocity (from D. G. Schleicher, PhD. dissertation, U. Maryland, 1982).

A series of observations of the OH radical in comet Halley are reported in the third chapter. These observations allow a map to be made, of the sunward velocity of the gas weighted by the density and averaged along the line of sight. Spherically symmetric outflow should produce well-ordered behavior in this map, like that shown in fig. 2. This study is the first attempt to investigate this basic assumption of cometary science.

A summary of the results of the two major chapters of this work is presented next. This section draws more general conclusions than can be drawn in reference to each paper alone.

Figure 1. OH Band Intensities and Ratios vs. Heliocentric Velocity

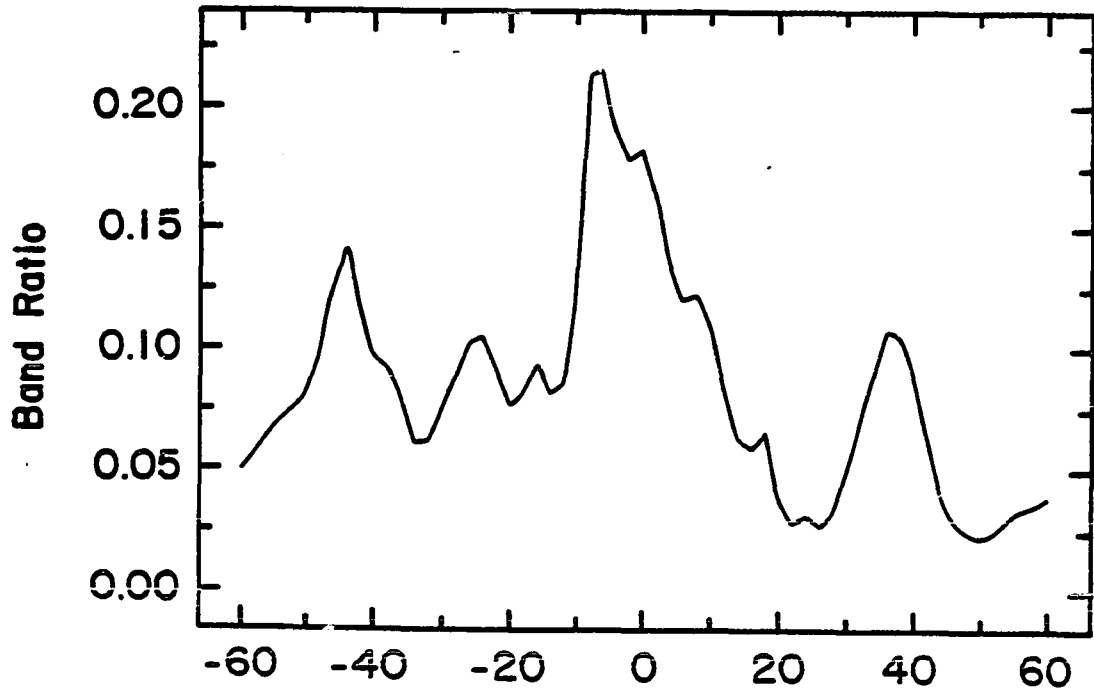
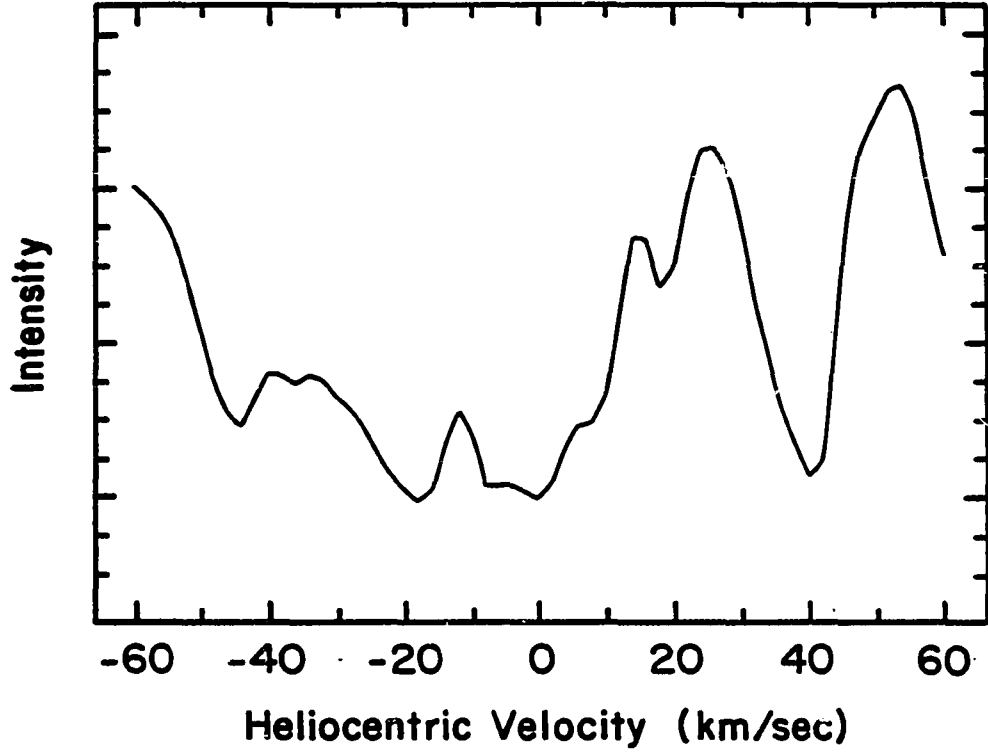
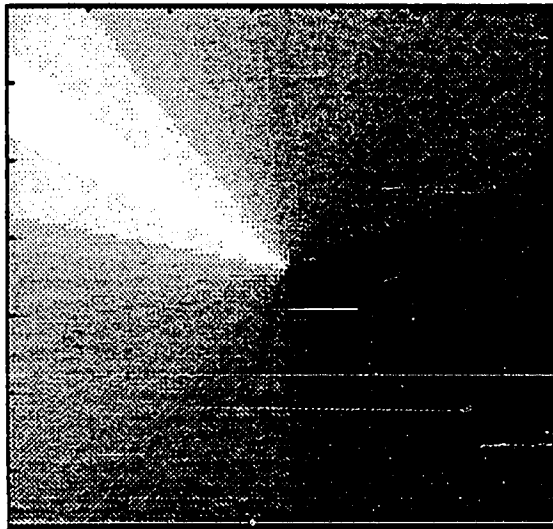


Figure 2-Calculated Ratio Image



The image processing procedure used in the third chapter is discussed in the appendix. The complexity of the procedure, the uniqueness of the data, and the poor quantitative agreement of the data with the theory merit a detailed discussion.

CHAPTER 2

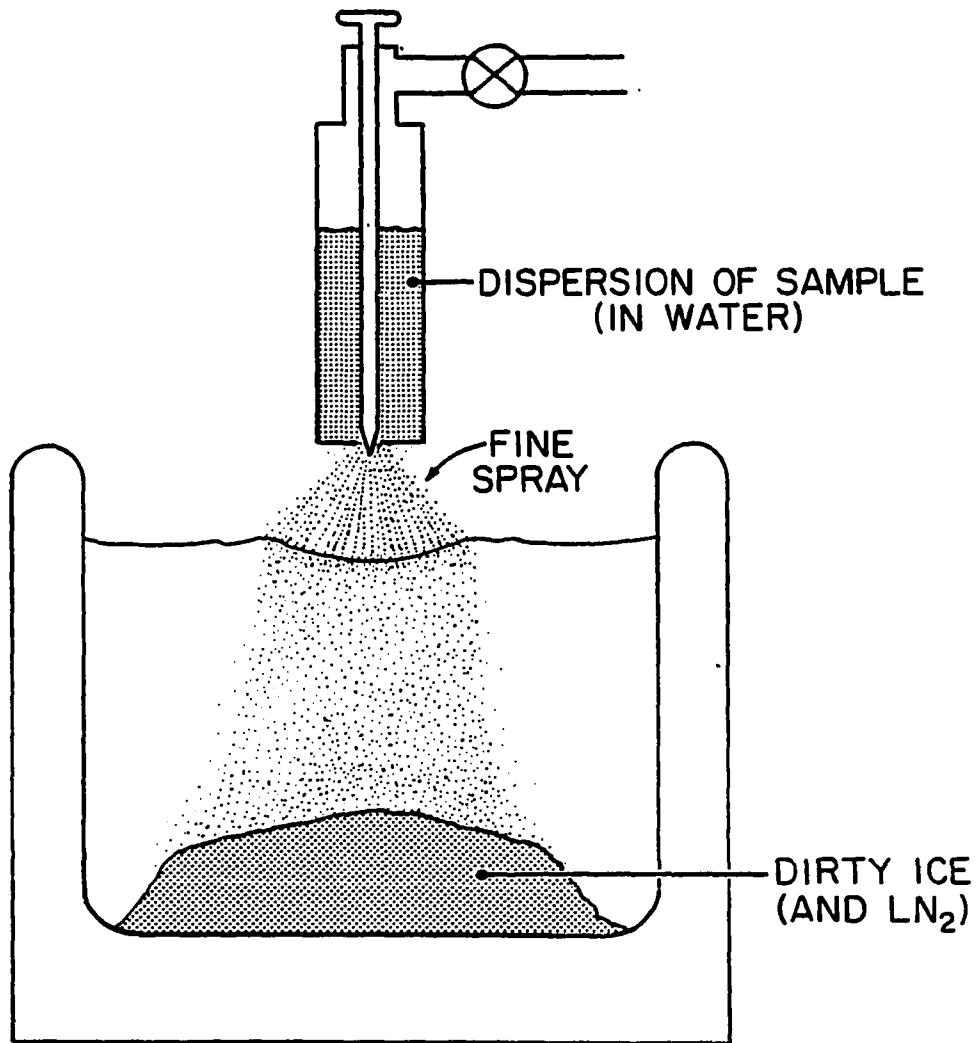
FILAMENTARY SUBLIMATE RESIDUE

This chapter is divided into six sections. The first discusses the details of the methods used to prepare the simulations. The second describes the results of the simulations which used only powdered minerals and water. The third section discusses the structure of silicate minerals and describes the suggested bonding mechanism responsible for forming FSR. The fourth section discusses the results of other investigators of interparticle bonding. The fifth section discusses the effects on the formation of FSR, of the inclusion organic (tarry) material in the simulation. The last section summarizes the results and discusses their applicability to real situations (Martian polar caps and cometary nuclei).

METHOD

Figure 3 shows the apparatus used to prepare most of the simulations. A sample of the mineral to be tested was ground with a mortar and pestle, and the resulting powder passed through a 100 μm mesh screen. A 2 per cent (by weight) solution of this dust in liquid water was prepared in a beaker, using a mechanical stirrer. All solutions were stirred for at least five minutes. The solution was then sucked into the spraying chamber through the orifice through which it would be sprayed, with the central needle removed. For almost all minerals, the largest particles remained in the beaker after the sample was sucked into the spraying apparatus. These dregs were not included in the simulation. The needle was then inserted into the orifice, a bottle of high-pressure gaseous nitrogen attached to the top of the spraying chamber, and the beaker in which the mixture was prepared replaced by a large dewar of liquid nitrogen (LN_2). The gas was then turned on and regulated to a pressure of 100-300 p.s.i. Lower pressures were used in later experiments, especially those involving pure phyllosilicates. This variation in pressure had no discernible effect on the process. The needle was then slowly removed, and the mixture

Figure 3--Simulations Apparatus



allowed to spray into the liquid N₂ bath. Upon leaving the orifice, the mixture atomized into droplets of about 10 μm in size. These froze instantly upon contact with the LN₂, and sank to the bottom of the dewar.

In most experiments, the "dirty snow", with a consistency like thick cream, was decanted into a precooled smaller dewar, along with an equal volume of LN₂. This dewar was then placed in a vacuum chamber, which was evacuated to a pressure of about 200 μm Hg. The liquid nitrogen solidified and the pressure decreased below 100 μm, and the solid N₂ sublimed away overnight. The water then began to sublime. Thermocouple measurements in some experiments indicated that water sublimation took place at a temperature of about 240^oK. Sublimation times ranged from 2 to 14 days, the longer times for samples forming filamentary sublimate residue (FSR). The samples were examined visually upon removal from the vacuum chamber, to determine if they had formed FSR. The sample was then removed from the dewar, and examined under a low-power dissecting microscope to check uniformity. Representative samples of raw and processed materials were mounted and examined in a scanning electron microscope (SEM). Almost all samples of FSR had a uniform grain size and structure throughout, with no differentiation of the sample apparent. Formation of FSR was always connected with a change in the appearance of the materials in the SEM.

The rate of delivery (spraying) of the mixture into the LN₂ could change the texture of the resulting FSR. If the delivery rate was too high, the frozen droplets coalesced into larger ice balls, which floated (for a time) on the LN₂. Upon sublimation, these balls tended to cling together fairly well, but the FSR produced was observed to be on the whole less cohesive than that produced by slow spraying. The apparatus needed constant attention to prevent ice balls from developing, and to maintain an even spray. Later simulations, especially those involving serpentine and vermiculite, used an improved apparatus which replaced the needle with a valve, which could be adjusted more exactly. Simulations made with this apparatus, involving minerals tested with the original apparatus, gave identical results.

RESULTS

Table 1 shows the results of processing different types of minerals in the manner previously described. It is clear that only some phyllosilicates (sheet silicates), exhibited any tendency to form FSR. Cab-o-sil is a special case, and will be dealt with separately.

Table 2 shows the results of a detailed investigation of the various kinds of phyllosilicates. The immediate observation is that FSR is formed by those minerals having some interlayer water, although most phyllosilicates were altered during the process. Specifically, the smectite clays montmorillonite and nontronite, vermiculite, and to a certain degree, the hydrous mica illite were observed to form FSR. Ordinary micas, represented by lepidolite, kanditic clays like kaolinite, and anhydrous phyllosilicates like pyrophyllite did not form FSR. Serpentine, a phyllosilicate formed by aqueous alteration of olivine and believed to be common in the matrix material of carbonaceous chondrite meteorites as well as on Mars (Singer, 1985), exhibited no tendency to form FSR.

Macroscopic examination of the FSR before its removal from the dewar showed that, in general, it retained the shape of the dirty ice originally present. In some cases, particularly when a dilute mineral mixture was used, the upper part of the FSR appeared to have pulled away from the sides of the dewar (Fig. 4). In most cases, however, the FSR was broken in mm-sized clumps. A sample of 1.5% montmorillonite in water was prepared, and sublimed in a petri dish. This procedure allowed observation of the formation of inhomogeneous material from originally homogeneous (on a mm scale) ice.

The impedance of gas flow by FSR was investigated by measuring the pressure drop across a sample while varying the flow rate of air through the sample. The sample was made in a five cm diameter tube. A four cm inside diameter annulus was attached to the end of this tube, to prevent the sample from slipping out. This tube could then be placed in another tube and the apparatus evacuated. Air admitted to one end of the apparatus must then flow through the sample to the lower pressure region on the other side. For samples thicker than one centimeter, the pressure drop stabilized at $\sim 200\mu\text{m}$ across the sample, for flow rates of up to 10^{19} molecules per sec per cm^2 . Only for flow rates below 10^{15} molecules per sec per cm^2 was there a linear response between pressure gradient and flow rate, as

Table 1

MINERAL TYPES		
Mineral:	Structure:	Forms FSR?
Forsterite	Nesosilicate (olivene) isolated SiO ₄ tetrahedra	No
Augite	Inosilicate (clinopyroxene) chains of SiO ₄ tetrahedra	No
Anorthite	Tectosilicate (feldspar) framework of SiO ₄ tetrahedra	No
Cordierite	Cyclosilicate rings of SiO ₄ tetrahedra	No
Ferroaxinite	Sorosilicate isolated Si ₂ O ₇ dimers	No
Montmorillonite	Phyllosilicate (smectite clay) sheets of SiO ₄ tetrahedra	Yes
Pumice	volcanic glass	No
Basalt	volcanic rock	No
Cab-o-sil	commercial glass smoke	Yes

Table 2

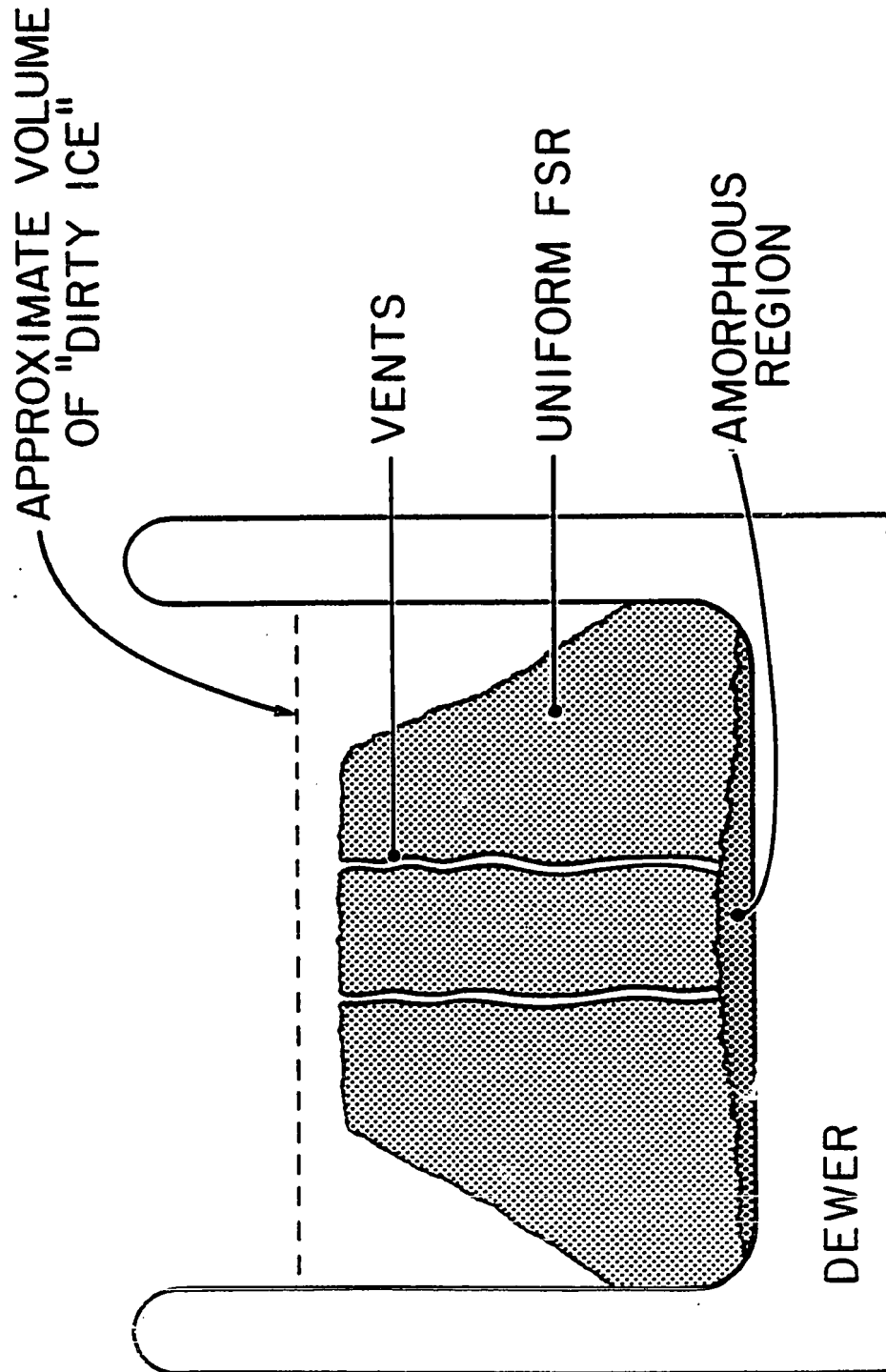
PHYLLOSILICATES

Mineral:	Structure:	Breaks Up?	FSR?
Lepidolite	2:1 mica (interlayer ions, no H ₂ O)	Yes	No
Illite	2:1 hydrated mica (interlayer ions, some H ₂ O)	Yes	Yes
Montmorillonite	2:1 smectite clay (much interlayer H ₂ O, ions)	Yes	Yes
Nontronite	2:1 smectite clay (much interlayer H ₂ O, ions)	Yes	Yes
Vermiculite	2:1 clay (very similar to smectites)	Yes	Yes
Kaolinite	1:1 clay (no interlayer H ₂ O)	Yes	No
Pyrophyllite	2:1 clay (no interlayer ions or H ₂ O)	No	No
Serpentine	1:1 clay (curved sheets, H ₂ O only adsorbed, not interlayer)	No	No

"Breaks Up?" refers to the formation of tactoids--"Does the mineral look different in the SEM after the process than before?"

"FSR?" refers to the formation of filamentary sublimate residue

Figure 4--FSR in Dewar



would be expected for Knudsen diffusion (Clifford and Hillel, 1986) of gas through a porous medium (D. Petrac, pvt. comm.). At higher flow rates, the pressure was high enough to allow the system to be treated as continuum flow. According to German (1981), in the continuum flow regime, the pressure differential should be proportional to the ratio of the flow rate to the average pressure. At near atmospheric pressures, the flow rate is directly proportional to the pressure, and so the pressure differential should be a constant, independent of flow rate. Thus the transition from Knudsen to continuum flow accounts for the bi-modal character of the flow rate vs. pressure differential plots. The low density (10^{12} cm^{-3}) and fairly high temperature ($\sim 200^{\circ}\text{K}$) of the gas near the nucleus give a mean free path of $\sim 10^2 \text{ cm}$. This large mfp indicates that Knudsen diffusion must dominate the gas flow through any realistic mantle.

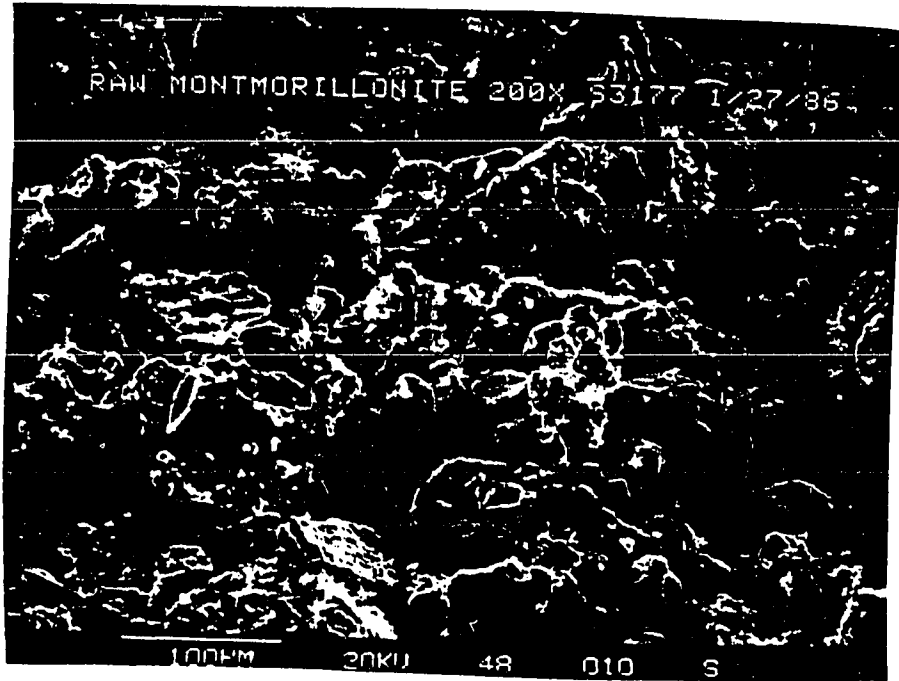
There is a marked difference in appearance in the SEM pictures, between the FSR and the residue left by minerals that didn't form FSR. Every mineral that formed FSR appeared to consist of much smaller, more uniformly sized units than the original powder (Fig. 5). SEM pictures of the raw powders show that the minerals have a size distribution from $<1 \mu\text{m}$ to $100 \mu\text{m}$, peaking toward the larger end of the size distribution. FSR appears to be made of micron-sized units welded together (Fig. 5e). The only minerals that didn't form FSR, but for which the appearance in SEM photographs changed markedly after processing, were lepidolite and kaolinite.

Isopropyl alcohol was used as an agent for transporting the montmorillonite, instead of water, in one experiment. The powder left upon sublimation of this mixture was again indistinguishable from the montmorillonite that was added in the beginning (no FSR formed).

The effect of liquid water on the formation of FSR was further tested by spraying pure water through the system into liquid N_2 , and separately adding dry montmorillonite powder. The montmorillonite thus was never exposed to liquid water. The powder left upon sublimation of this mixture was indistinguishable from the original powder (i.e., no FSR formed). Liquid water, mixed with phyllosilicates and flash frozen in small droplets, is necessary to form FSR on laboratory time scales.

Figure 5--Montmorillonite: Raw and FSR

a.



b.

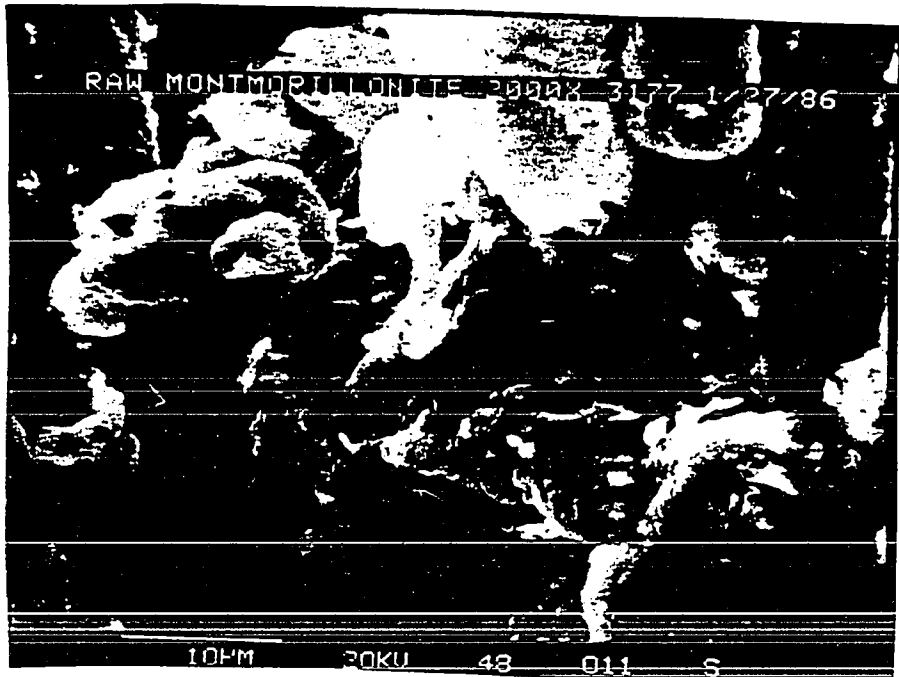


Figure 5--continued

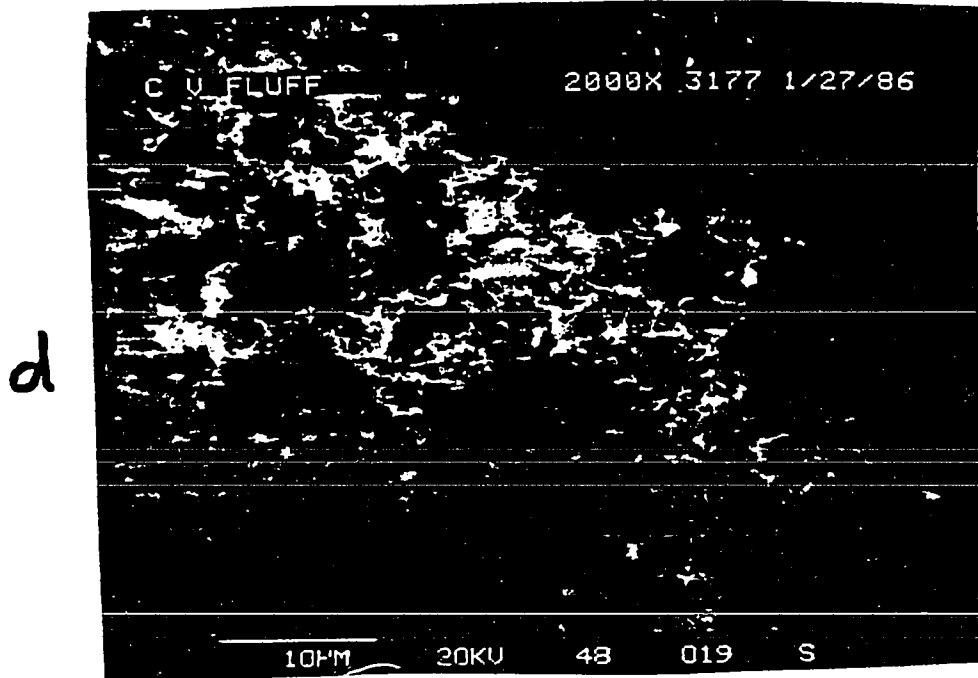
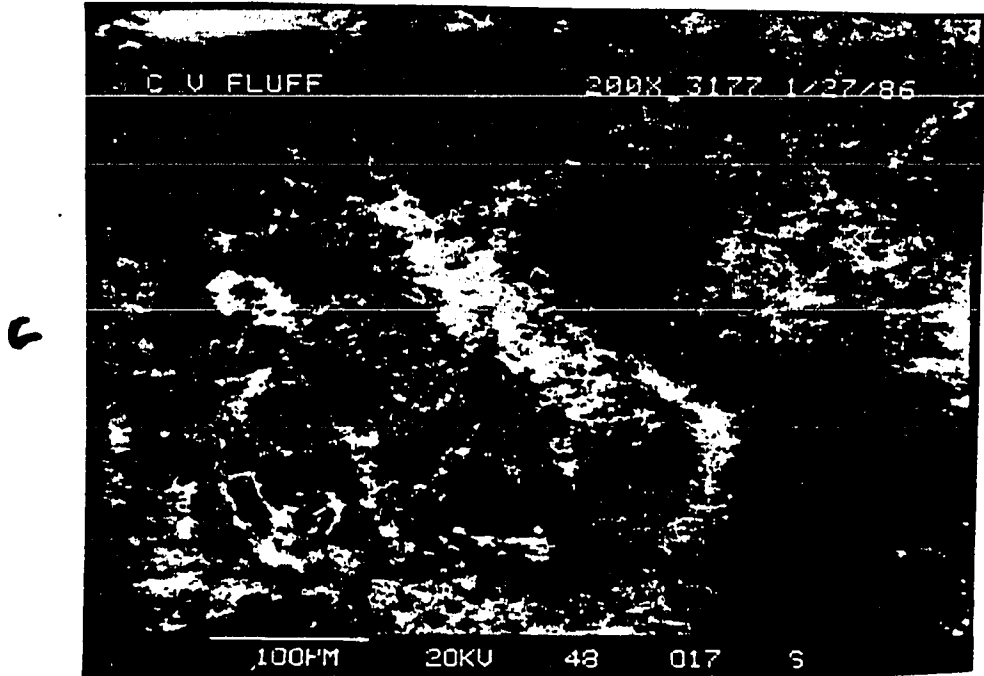
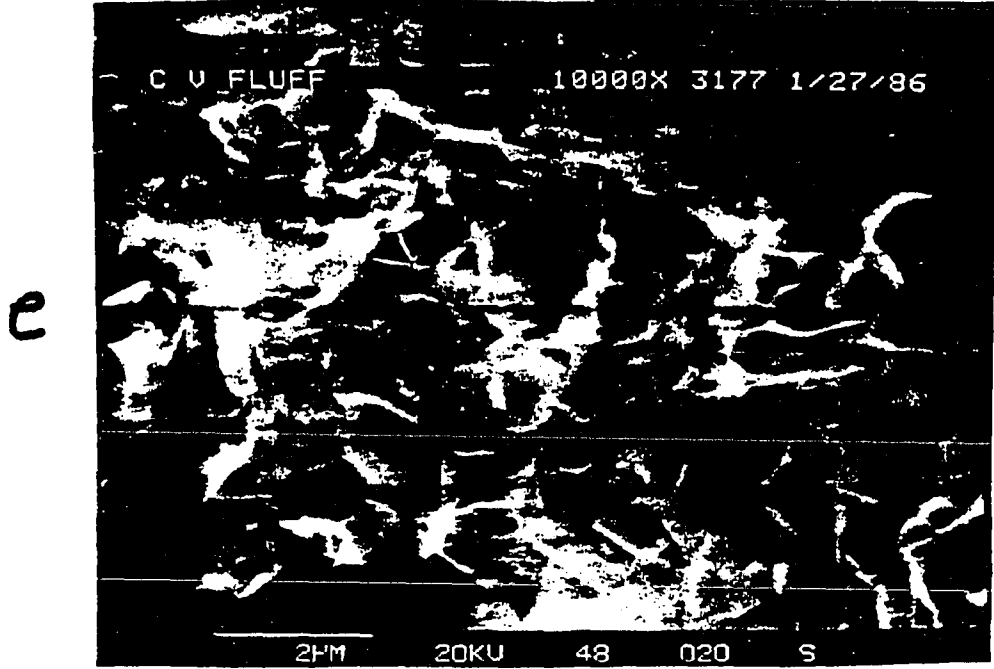


Figure 5--continued

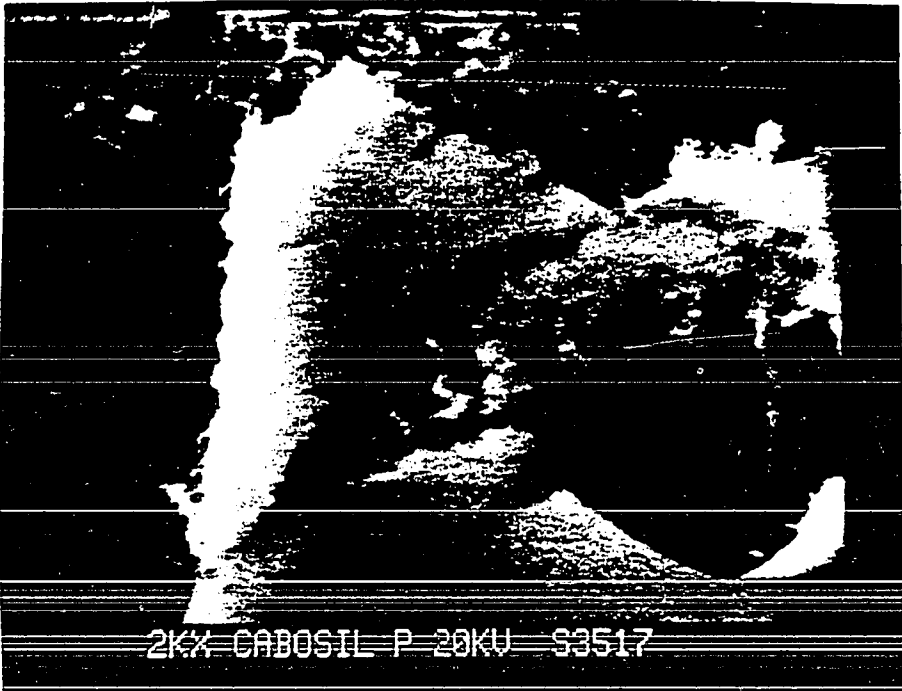
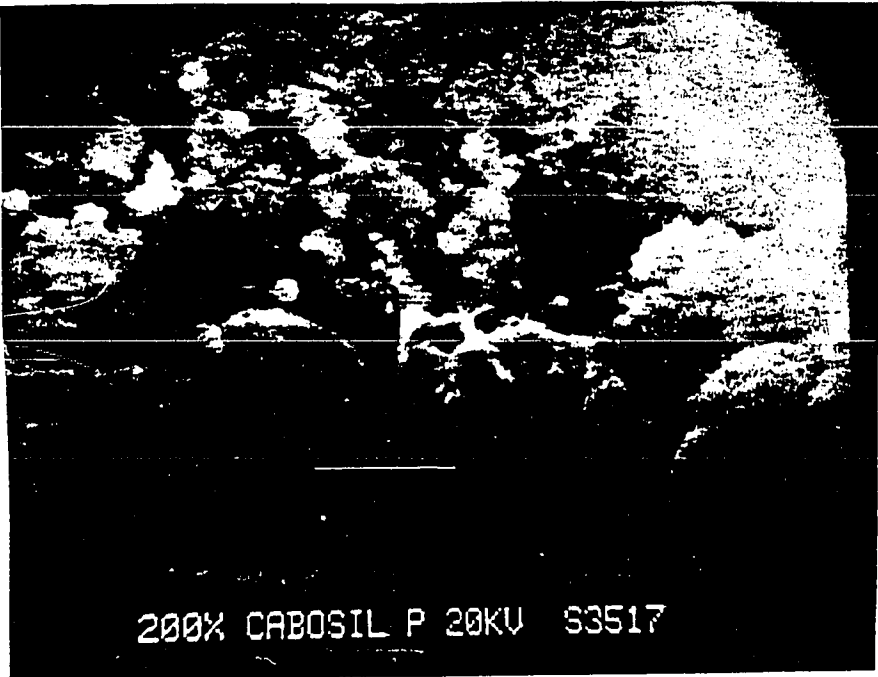


In a related experiment, FSR formed from montmorillonite in the usual manner (described above) was immersed in liquid N₂ and broken up mechanically. Pure water was then sprayed into this mixture, and the whole stirred again. Upon sublimation, a residue indistinguishable from the original FSR was formed. This was probably due to mechanical joining of irregular filaments of FSR upon sublimation of the water, although reformation of FSR in the normal manner cannot be ruled out.

We tested other materials for FSR formation. No materials besides Cab-o-sil, a commercial glass smoke, exhibited any tendency to form FSR. The Cab-o-sil grains are probably bound by electrostatic forces. The FSR formed from Cab-o-sil did not have the high tensile strength exhibited by that formed by the phyllosilicates, and charged up very readily in the SEM, indicating low electrical conductivity. Several coatings of conductive material were necessary to obtain the photographs shown in Fig. 6, which shows the more discrete nature of the grains in this FSR. The molecular structure of glass is, by definition, amorphous. This lack of crystal structure precludes the formation of FSR in the manner observed in the phyllosilicates (discussed below). Pumice (volcanic glass) and basalt (volcanic rock) did not form FSR. Both of these samples had a much larger grain size than did Cab-o-sil, that might impede any FSR-forming process. Cab-o-sil is an interesting example of an alternative interparticle force, to that which bonds pure mineral FSR.

We also tested the effects of mixtures of minerals on the formation of FSR. When various amounts of montmorillonite were mixed with anorthite (which does not normally form FSR, see Table 1) in ratios of 1:1 to 1000:1 (by weight) [anorthite:montmorillonite], FSR was formed in all cases. Not all the anorthite was bound up in the FSR, but in all cases a significant amount of anorthite was included. This demonstrates the ability of FSR to bind together small particles of minerals which would not otherwise bind together.

Figure 6--Cab-o-sil FSR



ANALYSIS

Phyllosilicate minerals are formed of sheets of SiO_4 tetrahedra joined in a plane at three of their vertices, in a hexagonal array. This layer is referred to as the tetrahedral or "t" layer. It is always found in coordination with another layer of oxygen atoms, hydroxyl radicals, and cations in an array of octahedra, which is therefore called the octahedral or "o" layer. Phyllosilicate minerals are formed by either a direct alternation of these layers, and are called t-o or 1:1, or by attaching an (inverted) tetrahedral layer to the other side of the octahedral layer and stacking, forming a t-o-t or 2:1 structure. Examples of these structures are shown in figure 7.

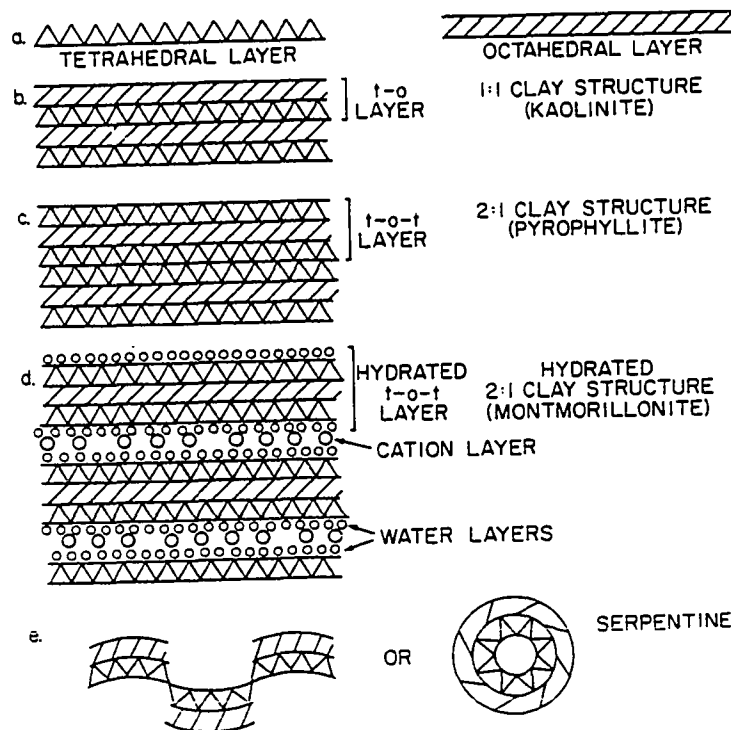
Most phyllosilicates, when mixed with liquid water, dissociate into stacks of t-o or t-o-t sheets or subunits of those sheets, breaking along the interlayer boundaries (Anderson and Banin, 1974). These stacks are called "tactoids". For montmorillonite, these tactoids tend to be 2-15 layers (30-100 Å) thick, and a few tenths of microns in extent. Montmorillonite and vermiculite tactoids are very elongated, having 700-800 m^2/gm of surface area. Tactoids of illite (a hydrous mica, see Fig. 7) are more massive, having only 100 m^2/gm , and kaolinite tactoids more massive still, with 25-50 m^2/gm .

The outer faces of these tactoids, which would normally have a single layer of water molecules bound to them in the case of hydrated silicates, attract more water molecules to them (when in solution). This effect can extend to several monolayers of water, before the unbalanced electric field from the silicate layers are effectively neutralized (Grim and Cuthbert, 1945). This water has "properties different from those of liquid water. It seems most likely that the water structure is generally similar to ice...the water might well be described as quasi-crystalline." (Grim 1968, p.246). When the dirty water droplets freeze, the expanding water crystal faces within the droplets force the silicate impurities ahead of them, until they are forced together between the adjacent crystal faces. There, the layers of unfrozen water bound to the tactoids allows the tactoids to coordinate and rebond into the original mineral. When the excess water is sublimed away, the mineral structure left records the crystal structure in the frozen droplet. Even small droplets (~1 μm in diameter) show this relic crystal structure, and did not solidify into amorphous ice upon introduction to the IN_2 bath. FSR which preserves the morphology of the ice

droplets is referred to as "botrioidal" FSR by Saunders et al (Fig. 8).

When the mineral is in so dilute an aqueous mixture that the tactoids generally encounter no other tactoids upon freezing, they remain unbound to other particles until the sublimation of the surrounding droplet frees them. The jostling from the subliming H₂O molecules ("wind") may cause the tactoids to move upon release from the ice, or the tactoids may just fall down, resting on the sublimation surface until they come into contact with other tactoids. The electrostatic forces caused by the unbalanced charges in these tactoids will then cause them to coordinate and bond together, and this bonded unit will then either blow around in the "wind" or fall down until they encounter the next particle. They will rapidly form a "net" of the original mineral which traps each tactoid as it is exposed, thereby preserving a semblance of the original shape of the sample, on a macroscopic scale.

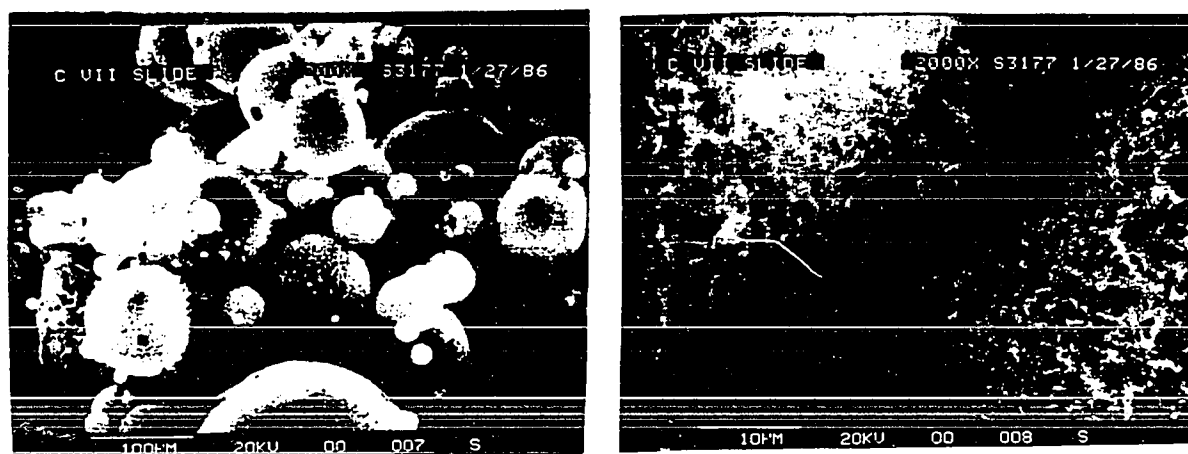
Figure 7. Silicate Mineral Structure



The advance of the sublimation front inward from the walls of the dewar, as well as down from the top of the ice, could explain the movement of the FSR away from the walls of the dewar (Fig. 4). At the start of sublimation the particles are released from their icy matrix and rest upon its (sloping) surface, falling away from the heat source (walls). When these particles contact other particles, they bond into a cohesive net of FSR. More newly released grains then move around until they bond to the bottom of the net. The net is in contact at some points with the ice and walls, and so does not continue to contract down onto the grains. The FSR is thus built from the bottom, and retains the outward appearance of an earlier position of the sublimation front.

The formation of FSR as mm-size clumps when high concentrations of minerals are used, is explained in a similar manner. As the top layer of ice sublimed, a layer of FSR formed, retaining the macroscopic shape of the original ice. As the sublimation front receded below this layer, the FSR impeded the outflow of the gas from the subliming ice, and a slight pressure gradient was formed. This pressure gradient broke the weakest bonds in the FSR, causing its comminution. The bursts of gas so released were frequently strong enough to project the mm-size clumps several centimeters above their original resting place.

Figure 8 Botrioidal FSR



Lepidolite and kaolinite did not form FSR but their dust grains did appear to have been broken into tactoids during processing. This behavior can be explained by their lack of interlayer water. As shown in Table 2, lepidolite is a mica: kaolinite is an anhydrous clay. Neither of the minerals unit cells has a net charge, and thus, although these minerals are broken up in liquid water like most phyllosilicates, the tactoids formed do not coordinate with each other to form FSR.

Not all phyllosilicates dissociate in water to form FSR. Serpentine and pyrophyllite (Table 2) are examples of this behavior. Referring to Fig. 7, we see that pyrophyllite is a very simple 2:1 clay, with no interlayer material. Thus, its structure is very compact and not very susceptible to aqueous alteration. Serpentine is a special case (Fig. 7e). Its structure is like that of a 1:1 clay, but the octahedral layer is markedly larger than the tetrahedral layer. Thus, the two-layer unit tends to bend noticeably, with a radius of curvature of about 100 Angstroms. The different petrologic types of serpentine are due to the different ways these units are put together: when the units are put together in such a way that the curves cancel, sheets are formed, much like curved Spanish tiles can cover a flat roof. If the units are put together in such a way that the curves are allowed to complete the circle, the mineral forms long thin tubes. Both forms have room in their structure to adsorb water, but no room for true interlayer water. Both pyrophyllite and serpentine are well bonded together, and have unit cells which are electrically neutral of themselves. They do not break into tactoids in liquid water, and so it is not surprising that they don't form FSR.

Saunders et al. inferred high electrical conductivity and tensile strength of FSR from SEM observations. They noted that the electron beam did not charge the sample, nor was the sample mechanically deformed, even after long periods of exposure in the SEM. We have confirmed these results, for, except for Cab-o-sil (a commercial glass smoke), all SEM pictures were made from samples were not coated with carbon to drain off the charge from the SEM beam. In high power SEM pictures of FSR (Fig. 5e), there appeared to be a fillet of material between subunits of mineral (indeed, it was sometimes hard to distinguish between subunits and bonds). We conclude that the FSR can be considered to be one mineral unit, not a conglomerate of many smaller units. The intergrain bonds are thus not purely elec-

trostatic, but ionic, explaining the high electrical conductivity of the unit. The FSR is not easily broken down into its constituent grains by mechanical means, as would be expected for grains held by electrostatic forces. Moreover, once broken up, the FSR does not reform itself, as would be the case if there were electrostatic forces between the particles. Crushed FSR forms an amorphous material very like that formed by crushing the original montmorillonite powder.

On the basis of these observations and explanation, we would predict that all hydrated phyllosilicates should form FSR upon mixing with liquid water, flash freezing, and the subsequent sublimation of the H_2O . In particular, other smectite clays and the hydrated form of kaolinite (halloysite) should form FSR.

A comparison of the process described here and those thought to occur in real situations can be made. The process of FSR formation in laboratory time scales appears to require the presence of liquid water at some point in the simulation. Liquid water is not likely to be present in either the Martian or cometary environments, although its presence in the past, particularly on Mars, is quite possible. As mentioned above, the tactoids formed from smectite clays upon introduction to liquid water surround themselves with a coordinated layer of water several molecules thick. This layer remains fluid well below freezing (Anderson, 1967). Smectite grains embedded in icy matrices would have some fluid water around them, which might allow them to coordinate and bond into FSR even in the absence of liquid water globally. This process would probably be much slower than that simulated in the laboratory, but the results over planetary time scales would be the same.

OTHER RESULTS

Other observations of interparticle forces have been made. Papers by Greeley (1979), Johnson et al. (1975), Greeley and Leach (1979), and Arrhenius and Asunmaa (1973) are discussed in this section, and the results compared with FSR.

Greeley (1979) reports aggregation of dry silt and clay particles into sand-sized conglomerates. He explains this agglomeration as electrostatic bonding. He measured an electrical current to flow between a barrier and ground, when his conglomerate particles are blown against the barrier. This current is induced either by friction between particles or between particles and the gas or by the comminution of the original particles. These conglomerates are much denser than FSR, and are formed without the presence of liquid water. Greeley observes that these particles are deformed by an SEM beam, but rebound to their original shape. They also break apart and reform easily, under mechanical (sonic) stress. No structures larger than a sand grain are formed, but this might be due to the formation method (wind tunnel). Greeley does not report the electrical conductivity of his samples, nor does he say whether he coated the samples with conductive material before introduction into the SEM.

FSR did not distort to any significant extent under an SEM beam, nor did it have to be coated to drain off excess charge during observation. It was not broken up under light (sonic) mechanical stress. Although it clings together after being broken apart into mm-size pieces, this behavior is probably due to mechanical interaction between filaments extending from adjoining particles as much as to electrostatic forces. The strength and cohesiveness of FSR as compared to Greeley's particles allows us to conclude that Greeley's agglomerate particles and FSR are not different examples of the same process.

Cohesive forces appear to be present in other simulations of Martian surface effects. Johnson et al. (1975) suggested that sudden desorption of CO₂ from grains that had been previously equilibrated with cold gas could inject the fine dust particles into the Martian atmosphere. This could happen either "explosively" or by formation of fissures and jets, depending on the rate of heating. These methods imply significant intergrain forces, to hold back or channel the escaping flow. Johnson et al. used an assortment of silica gel particles, and found that these effects were most noticeable when the smallest particles were concentrated near the surface. The bonding was probably electrostatic, as the disruptive forces were much smaller in his experiments than are needed to disrupt FSR. There was no liquid water present in his experiments, and silica gel probably won't form FSR anyway, as it lacks both crystalline structure and interlayer water. The simulation used too high CO₂ pressures and heating rates to be

strictly applicable to the Martian environment.

Greeley and Leach (1979) report a similar simulation to that of Johnson et al., using water instead of CO₂, as well as a variety of (larger size) particle types. Not surprisingly, they obtained results similar to Johnson et al, upon suddenly reducing the gas pressure over the hydrated beds. The particle compositions were not well characterized in their brief report, but it seems they used no materials similar to those used in our simulations. The fact that they used no liquid water, coupled with the "triggering" of outbursts they observed when passing a low-speed wind over the hydrated bed, leads to the conclusion that the interparticle binding forces they observed were not caused by an effect similar to that which binds FSR.

Arrhenius and Asunmaa (1973) report considerable electrostatic bonding of lunar dust. Their SEM photographs of this effect show the grains as distinct, individual units, with a minimum of contact between them. This is very different from the SEM photos of FSR we obtained (Fig. 5e), where each grain appears welded smoothly to the next, often with a "fillet" of material providing a larger bonding area than would be expected in the case of electrostatic bonding.

ORGANICS

To better simulate the cometary environment, we performed several simulations involving organic binding material. Interplanetary dust particles (IDP's or Brownlee particles) are believed to be the only samples of cometary material available for study (Brownlee 1985). Detailed analysis of these particles (Bradley and Brownlee 1986) shows that of the two types of chondritic stratospheric particles, only the "chondritic porous" (cp) type probably came from comets; the "chondritic smooth" (cs) type presumably came from the asteroids directly or formed by ablation during atmospheric entry of meteors coming from asteroids. Bradley and Brownlee describe a compositional distinction between these types: hydrated silicates occur only in cs particles. The olivine and pyroxene grains in Brownlee particles appears to be bound together by a matrix of "amorphous carbon", possibly the result of pyrolyzation of

organic material.

Additional justification for including organic materials in our simulations is the observation of pure organic particles in the vicinity of the nucleus of Halley's comet by the VEGA and Giotto spacecraft. Kissel et al. (1986a,b) report the discovery of a new class of small cometary particles made entirely of hydrogen, carbon, nitrogen and oxygen, which they term "CHON" particles. They made up a considerable fraction of the population of solid matter in the near nuclear region.

Gradie and Veverka (1980) discuss an additional observation relevant to the presence and composition of solar system organic material. Spectra of asteroids exhibit a downward trend in visual albedos and an increasing slope of the near IR spectra of the asteroids, as the semimajor axis (mean distance from the sun) of the asteroids increases. Gradie and Veverka explain this trend by postulating an increasing abundance of organic polymers (kerogens) in the makeup of the surface layers of the asteroids. They extrapolate these trends to infer that kerogens are probably an important constituent of cometary nuclei.

Several simulations were attempted using a coal tar residue (kerogen) similar to that described by Gradie and Veverka (1980). The method used in preparing our simulations requires the organic material to be liquid. Our attempts to make a fluid solution of this material failed, so we tried to make a simulation using kerogens indirectly. Basalt powder was mixed with the kerogens with a mortar and pestle, and the resulting powder mixed with pure water ice (prepared in the same manner as the other simulations) and sublimed, the original powder (kerogen and basalt) was left at the bottom of the dewar.

While liquid water is not believed to be present at any stage during the formation of the planetesimals in the PSN, more accurate simulations involving the condensation of gaseous water directly to solid are beyond the scope of this investigation.

Spacecraft observations of the nucleus of Halley's comet (Keller et al. 1987) revealed that it is very dark (a visual albedo of less than 5%). We simulated this material with a dark, organic, water soluble material, a commercial preparation called "Tree-heal". This is an emulsion of water, tar, and a few per cent montmorillonite clay, called "Tree-heal". The near-infrared spectrum of this material is

compared to that of D-type asteroids (from Bell et al. 1987) and cometary nuclei (Campins et al. 1987) in Fig. 9 (normalized at $\sim 2.3 \mu\text{m}$). The tar is redder than the naturally occurring objects. This observation follows the trend described by Gradie and Veverka described above. Comets are assumed to have formed beyond the asteroid belt, and so their spectra should be even more red than that of the asteroids, if this trend continues. The deep absorption bands in the spectrum of the tar are due to the water in the emulsion. Water is not nearly so abundant in the asteroids, so their spectra rarely show these bands.

To study the effect of montmorillonite on the tar mixture, a series of simulations involving various dilutions of montmorillonite and the tar mixture were performed. The FSR formed in all cases showed no systematic variations in macroscopic properties with the amount of montmorillonite used. Montmorillonite has no effect on the formation of FSR in the presence of organic binding material.

A similar dilution series was performed using basalt and the tar mixture. As mentioned previously, basalt does not form FSR in the absence of organics. It was found that the solid material had to be $\sim 15\%$ organics (by weight) in order to bind all the basalt into a block of FSR. The FSR formed was very porous ($\sim 95\%$ free space), and a good thermal insulator ($\sim 0.3 \text{ ergs}/(\text{cm}^2\text{K})$). Fig. 10 shows that the FSR formed with organics was much blockier (less filamentary) than that formed by minerals alone. The average pore size was about $10 \mu\text{m}$, much larger than that in pure mineral FSR. The density of organic-basalt FSR (0.1 gm per cm^3) is $\sim 10\times$ that of pure mineral FSR. Note that smaller fractions of organics caused some cohesion, but did not form a continuous block of FSR. FSR formed with smaller amounts of organics tend to consist of less porous, bulkier agglomerations of dust particles than the FSR formed with larger amount of organics.

Not all organics have the same abilities to form FSR under laboratory conditions. FSR is formed by volatile-rich organics (tar and water emulsions), but not by more refractory organics (kerogens). Comets are noted for retaining large amounts of water, however, and kerogens on the surfaces of asteroids may not reflect the composition of organics in cometary nuclei as well as commercial preparation does. Processes forming the organic compounds may have been very different in the outer (colder, less dense) PSN than in the inner regions, where the asteroids formed. Long term exposure to fairly

Figure 9--Spectrum of Organic Material

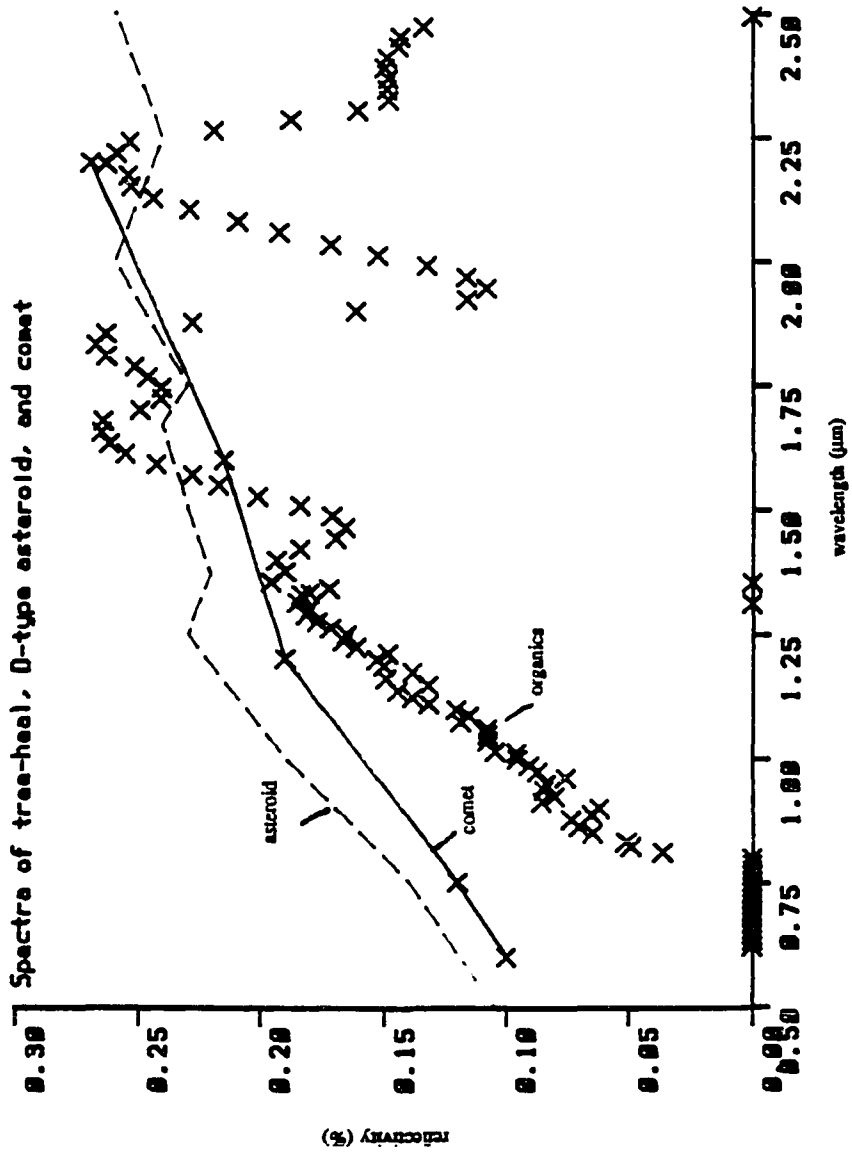
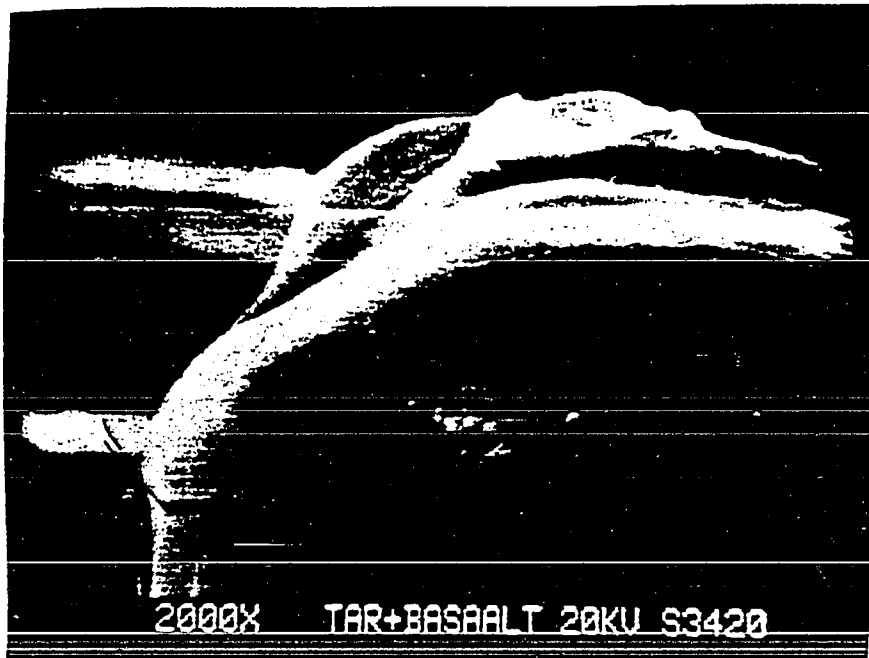
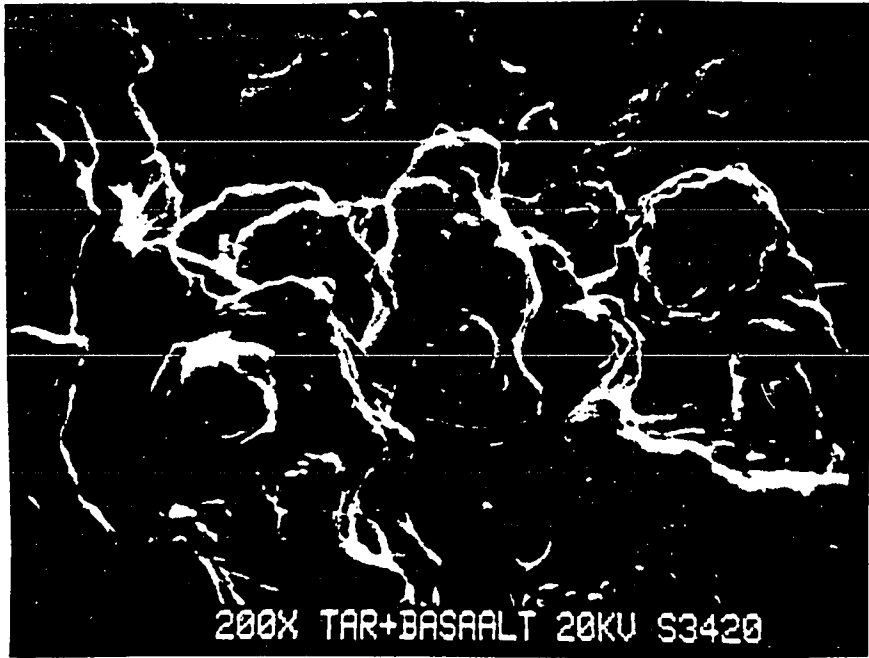


Figure 10--Organic FSR



intense sunlight and solar wind may have altered the organics on the surfaces of asteroids, as well.

The amount of organic material in those simulations that formed FSR is generally greater than Brownlee (1985) observes in his particles. Brownlee's particles are the ones blown free of cometary nuclei, however, and so are necessarily different from materials that remain on the nuclear surfaces. Particles exposed on parts of the nucleus which have high amounts of organic material will be bound to each other much more strongly than particles on areas with less organic material. These latter would then be preferentially blown free of the nucleus and, potentially, collected on Earth. If well bonded, organic rich particles are ejected from the nucleus, they are likely to be much larger and stronger than Brownlee particles, and would burn up upon atmospheric entry.

Even if cometary organics resemble kerogens, organically-bonded FSR might still form. The temperature of formation of the FSR should be taken into consideration (R. Johnson, pvt. comm.). Thermocouple measurements showed that FSR formation in the laboratory took place at temperatures of $\sim 240^{\circ}\text{K}$. At temperatures of $\sim 350\text{--}400^{\circ}\text{K}$, which were observed by the VEGA spacecraft on the nucleus of Halley's comet (Emerich et al., 1986) and predicted for the subsolar point of the nucleus by comet nucleus models (Fanale and Salvail, 1987), even kerogens should be fluid, with increased adhesive properties. Temperature of formation, as well as composition, should be important in the accurate simulation of the cometary environment.

DISCUSSION

The physical properties of FSR are listed in Table 3. The density was measured by weighing a sample of FSR and measuring its volume. The pore size was estimated from SEM photographs of the FSR. Continuum gas flow through a mantle of FSR would take place preferentially through the larger pores; smaller pores would have little effect on gas flow. The porosity was estimated by comparing the density of the FSR to the bulk density of its constituent materials. An absolute measurement of the tensile strength of FSR was not possible, however, a 1 cm thick sample 4 cm in diameter withstood a pres-

Table 3

PROPERTIES OF FSR

	Montmorillonite	Tar & Basalt
Density:	0.025 gm/cm ³	0.093 gm/cm ³
Pore size:(a)	1-10 μm	10 μm
Porosity:	99%	97%
Tensile strength:(b)	>150 gm/cm ²	>>mont. FSR
Thermal conductivity:	4.8x10 ⁴ erg/cm sec °K	1.3x10 ⁴ erg/cm sec °K

(a): average pore size for bulk sample--true FSR has smaller pores than botriodal FSR.

(b): 1 cm thick sample of FSR, 4 cm in diameter withstood a pressure differential of greater than 2.6x10⁻³ atm.

sure differential of 200 μm , much greater than would be expected to occur naturally. (Small particles may be broken free of the larger substrate, however. A subliming surface of botrioidal FSR was observed to project mm-size particles of FSR a distance of several cm, indicating that FSR bonds can be broken under laboratory conditions.) The thermal conductivity was measured by observing the equilibrium temperature of a metal plate on top of a sample of FSR, which in turn rested on another plate, atop a refrigerant. The equilibrium temperatures of the plates, the surroundings of the upper plate, and the thickness of the sample combine to give the thermal conductivity of the sample.

Although most of the original silicates in comets and the Martian polar caps were probably pyroxene and olivine, some might have been weathered over long periods of time to hydrated phyllosilicates. The hydration of mineral grains in ice has been discussed by Rietmeijer (1985). He observes that since the presence of an impurity lowers the freezing point of the surrounding water molecules, prolonged exposure to ice may hydrate otherwise anhydrous minerals. He cites several references to this process that occur in Antarctic soils. Phyllosilicates could form FSR upon subsequent sublimation of the water ice. The FSR so formed would be atypical compared to Brownlee particles, which have only small proportions of phyllosilicates.

FSR formation in laboratory time scales requires liquid water at some point in the simulation. However, over longer time scales, FSR can be formed without liquid water. One or two layers of adsorbed water around tactoids can exhibit the properties of a supercooled liquid down to temperatures of -70°C , including ionic conductivity comparable to that of liquid H_2O (Anderson, 1967). This fluid layer may allow phyllosilicate tactoids to coordinate and bond together, even when embedded in an icy matrix. FSR may therefore form on Martian polar caps and on cometary nuclei (although the presence of phyllosilicates in comets is undemonstrated).

Malin (1986) reports the existence of a significant amount of low density material in the Martian north polar region. He interprets it as dirty ice, with the ice forming at least 2/3 of the mixture. The entrained dust probably consists of fine weathering products brought to the pole during global dust storms (Pollack and Toon 1982). Such products probably contain a significant amount of clay, although

it is probably amorphous rather than crystalline (Singer 1985). The behavior of amorphous clays in subliming dirty ice has not been investigated, but our simulations indicate the possibility of this material binding together to form a protective refractory layer during periods of sublimation. This layer would protect the underlying icy layers, and could account for the observed stepped terrain (Howard, Cutts, and Blasius, 1982).

Bistatic radar observations of the north polar region (Simpson and Tyler 1981) revealed interesting behavior on the Martian polar cap. Observations made with the beam incident at a grazing angle to the cap gave a much lower value for the dielectric constant of the cap than those made with the beam normal to the surface. These observations may indicate a thin layer of material on the cap, with very different properties from the bulk of the cap. Although no measurements were made of the dielectric constant of FSR, its presence (or that of an analogous material) might explain these results.

The Martian polar regions are ringed by what appear to be fields of sand dunes. Sand dunes are not expected to form from particles as small as those observed at the Viking lander sites. The possibility of aggregates forming in the manner described above was first put forward by Saunders et al. (1984). The formation of large, low density grains by this bonding mechanism is attractive, but does not explain the dark color and presumably basaltic composition of the dunes. The low thermal conductivity of the FSR also seems inconsistent with the thermal inertia of these dunes, which is compatible with ordinary sand grains (P. Christiansen, pvt. comm.)

The presence of organic materials in cometary nuclei can be inferred from many observations. The "amorphous carbon" observed in interplanetary dust particles (IDPs or "Brownlee particles"), which binds the IDP's constituent mineral grains together, probably results from the pyrolyzation of organic material. The observation of organic "CHON" particles (Kissel et al. 1986a,b, Clark et al. 1987) and of the 3.4 μm "=C-H stretch" spectral feature (Knacke et al. 1987, Tokunaga et al. 1987) in Halley's comet also points to the presence of organics there. Cyanogen jets in the coma of Halley's comet are interpreted as coming from subliming organic dust particles (A'Hearn et al. 1986, A'Hearn et al. 1987, Samarasinha et al. 1987).

Models of cometary nuclei (e.g., Fanale and Salvail 1984, Brin and Mendis 1979, Podolak and Herman 1985) have generally assumed that no interparticle binding force exists at the surface of cometary nuclei. Recent observations of Halley's comet show that the nuclear size predicted by these models was too low, and that cometary nuclei do indeed appear to have volatile-poor mantles over much of their surfaces (Keller et al. 1986, Reitsema et al. 1987). The presence of these mantles gives some relevance to our simulations of cometary situations with organic materials that form FSR. The behavior of different types of organic materials needs to be investigated more thoroughly, however, before any definite conclusions can be drawn.

Additional evidence for the formation of refractory mantles on cometary nuclei was provided by the Dust Impact Detection System (DIDSY) on the Giotto flyby of Halley's comet (McDonnell et al, 1987). The mass spectrum of the dust observed near the nucleus was found to be much more strongly biased toward larger grain sizes, indicating the dominant presence of larger grains near the nucleus. Earth-based observations of primitive meteorites and (cometary) Brownlee particles show them to be made of agglomerates of much smaller particles. If the large particles suggested by the DIDSY observations were not atypical compared to those particles observed on Earth, the DIDSY particles must be sizeable agglomerations of smaller grains. These agglomerations may be fragments of larger agglomerations, or have broken away from a continuous mantle on the nuclear surface.

We have defined some grain-binding processes that might be important in explaining some observations of cometary nuclei and Martian polar terrain. We have produced filamentary sublimate residues that are stable under a wide range of conditions. These residues are highly porous, mechanically resilient, electrically conductive, and are excellent thermal insulators. We have demonstrated that, of the silicate minerals, only hydrated phyllosilicate powders bond together to form filamentary sublimate residues. Our simulations involving organic materials can produce similar residues, but there may be a dependence on the formation of FSR with the type of organic involved: emulsions of tar and water (which were fairly fluid at room temperature) formed FSR, while relatively refractory kerogens (which were quite hard at room temperature) did not. Both organic materials and clean, hydrated phyllosilicate

powders show some ability to bind together mineral grains which would not bind together by themselves. Not enough is known about the detailed composition of Martian polar terrain and cometary nuclei to warrant a more detailed comparison with our simulations.

CHAPTER 3

GREENSTEIN EFFECT

This chapter describes the observational part of this investigation. The gas in cometary comae is excited directly by sunlight. That flowing towards the sun is excited by a solar spectrum that is blue-shifted with respect to the spectrum exciting the gas flowing away from the sun. If the solar spectrum is discontinuous in the wavelength region which is exciting the molecule, large differences in exciting flux may occur for small changes in gas velocity. The Greenstein effect is caused by this differential excitation of the gas in the cometary coma. In particular, Schleicher and A'Hearn (1982) report the results of calculations of this effect in the $A^2\Sigma^+$ to $X^2\Pi$ transition of OH. This chapter describes the effort to image the morphology of gas flows in the inner coma of comet Halley, and interpret them with respect to this theory.

MODELING

An example of the expected results from observations of this effect is shown in Fig. 2. This image was made by assuming spherically symmetric expansion at a uniform velocity v , with no creation or destruction of the gas. Each pixel represents a line of sight (LOS) through the coma. For each LOS, the flux in a given band is given by the integral along that LOS of the emission efficiency times the local gas density. The gas density ρ decreases as d^2 , where d is the distance of the segment of the LOS in question from the nucleus. The emission efficiency depends on the sunward component of the velocity of the gas, which is the vector dot product of the gas velocity (in the radial direction) with the sunward direction. If a is the distance along the LOS from the point in question to the "plane of the sky" (the point on the LOS closest to the nucleus), v_s is the sunward component of the expansion velocity of the gas at the point along the LOS, and $f(v_s)$ is the emission efficiency at that heliocentric velocity, the intensity in a given band in a given pixel is:

$$I = \int \rho_0 d^{-2} f(v_s(a)) da \quad (1)$$

If the curves in Fig. 1 are assumed to be piecewise continuous, for each range of velocities, $f(v_s)$ can be assumed to be linear, with a slope of m and an intercept of b (m, b constant for the small range of velocities considered). Consider a cartesian system, with the origin defined at the nucleus, the z -axis parallel to the LOS, and the x and y axes in the plane of the sky, (lined up north-south and east-west for convenience). The sunward velocity v_s may be treated as three components. If v_x is the component of the sunward velocity parallel to the x -axis, and v_y and v_z similarly defined, then equation 1 becomes:

$$I = \int \rho_0 d^{-2} (m(v_x + v_y + v_z) + b) da \quad (2)$$

which breaks down into four integrals, and can be solved:

$$I = \frac{\rho_0}{w} (2mv \sin(\phi) (\cos(\theta)\cos(\beta_0) + \sin(\theta)\sin(\beta_0)) + \pi b) \quad (3)$$

where w is the minimum distance between the LOS and the optocenter, ϕ is the angle between the z -axis and the sunward direction (measured around the origin), β_0 is the angle between the x -axis and the projection onto the plane of the sky of the sunward direction, and θ is the angle between the x -axis and the line of sight in question. The intensity in each band is inversely proportional to the distance from the optocenter, as is expected for uniform outflow, with no creation or destruction of molecules (see Storrs et al. 1985 for discussion). Since ρ_0 (the gas density at the nucleus) is a constant, the first term divides out in the ratio of the fluxes received in each band, leaving the OH(1-1):OH(0-0) band flux ratio constant with distance from the optocenter, depending only on the azimuthal position of the pixel and the sunward direction (see Fig. 2).

The OH molecules are created so near the nucleus that there is no observable rise in OH density, (and hence brightness), away from the nucleus (optocenter) in these images. The field of view is small enough that the slow destruction of OH doesn't significantly alter the observed distribution. This model is therefore a reasonable prediction of the ratio image for a quiescent, spherically symmetric coma.

The effect of jets with different velocities and densities than the neighboring gas in the coma would be to project a region of different ratio on top of the fairly uniform spherically symmetric ratio of most of the coma. Inhomogeneities of this sort are seen in some post-perihelion observations.

OBSERVATIONS

The observations were made at the University of Hawaii 2.24m telescope at Mauna Kea Observatory (MKO). The detector was the Galileo/IfA Charge Coupled Device (CCD) (Hlivak et al. 1982). The pre-perihelion observations were made at the direct cassegrain focus, and have a field of view of 70 arcsec. The post-perihelion observations used a UV transmitting $f/4.5$ focal reducer, which gave a field of view of 140 arcsec.

The filters used to isolate the OH bands are described in the appendix.

Table 4 shows the dates, times, and filters used for all observations. Tracking rates were set and adjusted until the telescope followed the comet with a minimum of trailing. The results of this tracking procedure, which were usually quite satisfactory, are described in the fourth column of Table 4. Each pixel was 0.28 arcsec preperihelion, and 0.54 arcsec postperihelion. As the data was smoothed and binned during reduction, the spatial resolution was never better than ~ 1.5 arcsec, so the small amounts of trailing observed did not effect the results. Note that the pixel sizes in the images shown here (Fig. 13) are larger than those in the original images, as the data was binned to improve the signal to noise in the ratio images.

Pre-perihelion exposure times were generally 20-30 minutes, while exposure time around perihelion (January and March) were 10-20 minutes. The April images were averages of two 5 minute exposures in each filter.

IMAGE REDUCTION

Preparation of the ratio images required 11 processing steps, after obtaining the raw images. These steps were (in order): bias subtraction, flat fielding, interpolation over chip defects, removal of

Table 4

HALLEY OH DATA				
DATE(UT)	TIME(UT)	FILTER	COMMENTS/INTERPRETATION	EXCESS?
24 Oct	12:53-15:21	OH0,OH1,UVC	OH1 trailed 2-3 pixels W Spherical symmetry	YES
18 Nov	11:17-14:49	OH0,OH1,UVC	OH0 trailed 10 pixels NNE OH1 trailed 8 pixels E Spherical symmetry, rotation?	NO
21 Nov	8:55-10:08	OH0,OH1,UVC	OH0 trailed 3 pixels W OH1 trailed 3-4 pixels ESE Spherical symmetry, rotation?	YES
20 Dec	5:04-7:28	OH0,OH1,UVC	Spherical symmetry? (interpretation unclear)	YES
4 Jan	4:39-5:56	OH0,OH1,UVC	Spherical symmetry	YES
5 Jan	5:29-5:56	OH0,OH1,UVC	OH1 trailed 6 pixels NE UVC trailed 2 pixels SW Spherical symmetry	NO
6 Jan	4:57-5:21	OH0,OH1,UVC	Spherical symmetry	NO
7 Jan	4:45-5:10	OH0,OH1,UVC	Spherical symmetry	YES
8 Jan	5:08-5:34	OH0,OH1,UVC	OH1 trailed 2 pixels NW Spherical symmetry, possible turbulence	NO
4 Mar	15:47-16:20	OH0,OH1,RC	OH0 trailed 2 pixels SW OH1 trailed 2 pixels N Spherical symmetry	YES
5 Mar	15:38-16:10	OH0,OH1,RC	bad focus, hair in image* Interpretation unclear	NO
7 Mar	15:39-16:18	OH0,OH1,RC	Non-uniform outflow, sunward jet	YES
9 Mar	15:31-16:03	OH0,OH1,RC	Asymmetric outflow	NO
18 Apr	9:29-9:50	OH0,OH1,RC	multiple internal reflections* Rotation?	YES

* partially compensated for during image processing

OH0 means the 50A wide filter covering the OH (0-0) band

OH1 means the 50A wide filter covering the OH (1-1) band

UVC means the IHW 3640A continuum band (90A wide)

RC means the IHW 6940A continuum band (90A wide)

Note that images in Nov. and April were taken at opposition, with the sunward direction ill-defined.

Note that images were obtained through all the IHW filter on most nights.

Note that images in March were taken at a local minimum in the OH ratio, making interpretation difficult.

cosmic ray strikes, alignment of optocenters, correction for atmospheric extinction, smoothing, removal of sky contamination, differential sensitivity correction, removal of continuum contamination, and ratioing. The details of the image reduction procedure are discussed in the appendix.

OH1 EXCESS

The OH (1-1) image would sometimes develop a depressed area around the central peak, below the (scaled) (0-0) profiles, during the continuum correction procedure (fig. 11). This enhanced peak in the OH (1-1) image was not uncommon after continuum correction, and its occurrence is noted in the last column of Table 4 as "OH1 EXCESS". The fact that this excess did not appear on all nights indicates that it is not induced by errors in the image reduction procedure. The comet's water production rates varied from day to day (see, e.g., Weaver et al., 1986, Gerard et al., 1987), and the effect is observed only in the very innermost parts of the coma: when the observations coincided with an outburst of water production, the excess was seen, but under relatively quiescent conditions, the excess was too small to be observed. This effect could be used as a very sensitive measure of the activity of the comet, over short time scales.

Bertaux (1986) suggests that as water dissociates into H and OH radicals, the OH is left in a excited state. These states are not normally populated in radiative equilibrium of OH with sunlight. The radiative decay transitions from these excited states in the (0-0) band have wavelengths coincident with the (1-1) band. Where water is dissociating, the OH (1-1) band should be markedly brighter than normal. The guiding errors mentioned earlier do not allow a detailed interpretation of the dissociation region, but Fig. 12 shows the OH (1-1) image from Jan. 7, when this excess was observed. The corresponding scaled continuum image was subtracted, as was the corresponding OH (0-0) image, which was scaled to match the wings of the (1-1) image. This process removed both the continuum sunlight reflected off dust grains in the inner coma, and the equilibrium OH light. Figure 12 is therefore an image of the light from OH radicals excited directly during decay of water--the first direct image of the dissociation region, if this interpretation is correct.

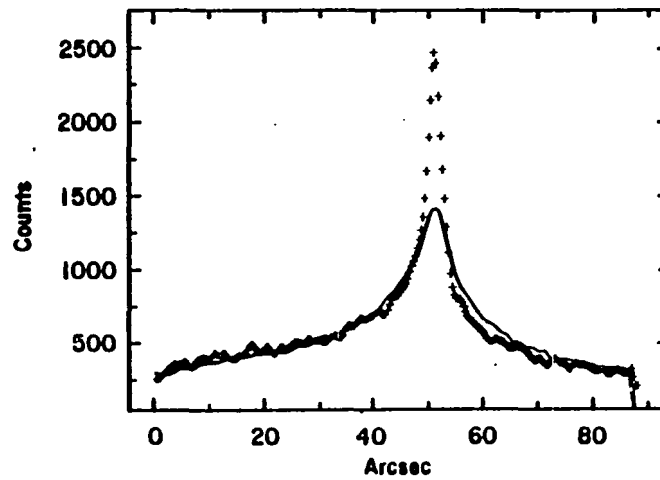
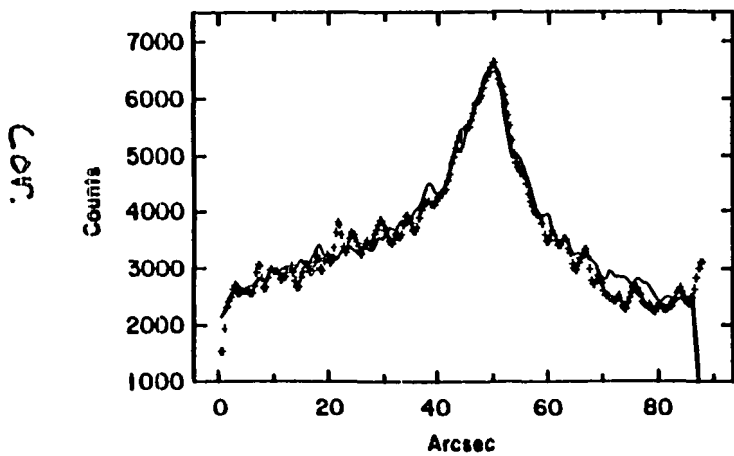
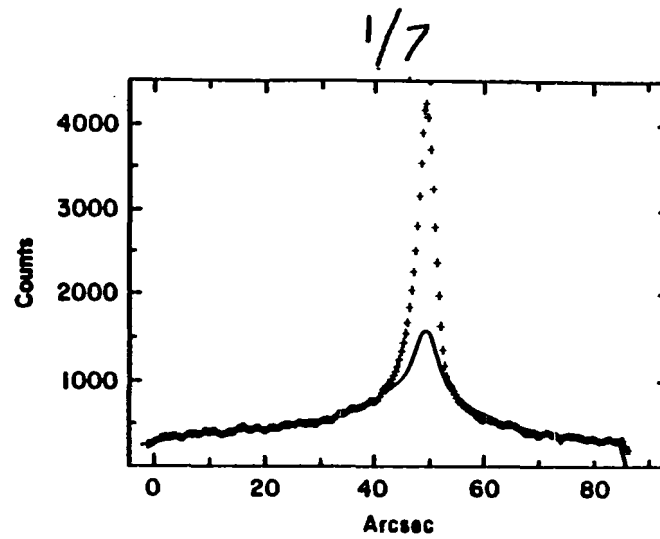
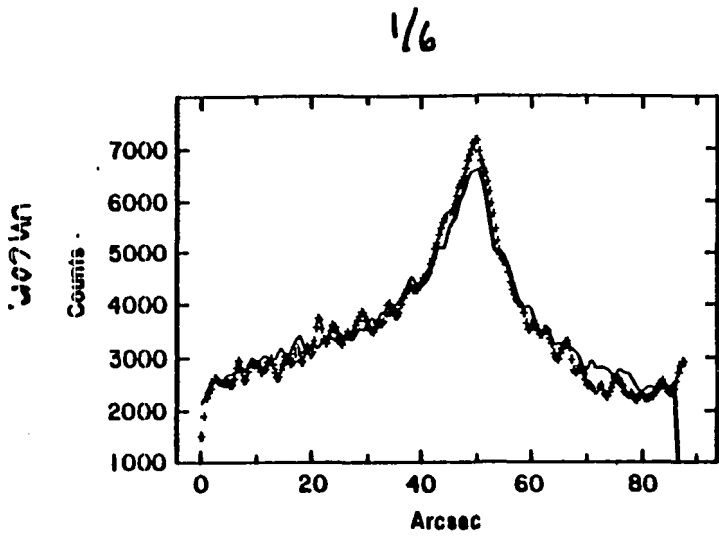


Figure 11--Image Profiles

Figure 12--OH1 Excess Image



RESULTS

The fourth and fifth columns of Table 4 summarize the basic results of this investigation. Spherical symmetry is generally the rule in the pre-perihelion observations, and in April. In March, however, significant non-uniformities are noticeable. Distinct dust jets and highly variable morphologies were noted by many observers during this time (M. Combi, pvt. comm.).

Figure 13 shows the ratio images for each night that OH data was obtained. The image scale, optocenter position, and sunward direction are also indicated for the ratio image. In all cases, north is to the top, and west is to the right. Heliocentric velocity and positional information (to calculate the sunward direction) were taken from Edberg (1983). As the morphology of the images varied from night to night, each observation will be discussed separately, with more general results discussed at the end of this section. Note that the images are shown in reverse coloration, with white indicating low values and black indicating high values. Also shown are conventional contour plots of the ratio images.

October 24: the sun is to the south-east. The ratio image has lower values, of about 0.18, to the south-east, and higher values, about 0.23, to the north-west. The overall morphology is indicative of spherically symmetric outflow of OH. However, according to the predictions of Schleicher and A'Hearn (1982) (Fig. 1), the ratio should be near a local maximum, with values around 0.10 to 0.11, when the comet has a heliocentric velocity of -24 km/sec.

November 18: the comet is at opposition to the sun. The ratio image has lower values of about 0.22 to the east, and higher values of 0.30 to the west. These ratio values are much higher than predicted by Schleicher and A'Hearn (Fig. 1) for a heliocentric velocity of -25 km/sec. Their calculations put the ratio near a local maximum with predicted values of 0.10. The existence of a gradient in the ratio image at low phase indicates some differential bulk motion of the gas in the inner coma.

November 21: the comet is still at opposition. The ratio image shows a region of lower values (~ 0.20) to the south-east, and higher values (~ 0.22) to the north-west. The small phase angle (6 degrees) would tend to mask the effects of spherical symmetry, yet the range of ratio values indicate a very large range of projected sunward velocities (see Fig. 1). The ratio values are still predicted to be at a local

Figure 13--OH Ratio Images, Contour Plots, and Continuum Images

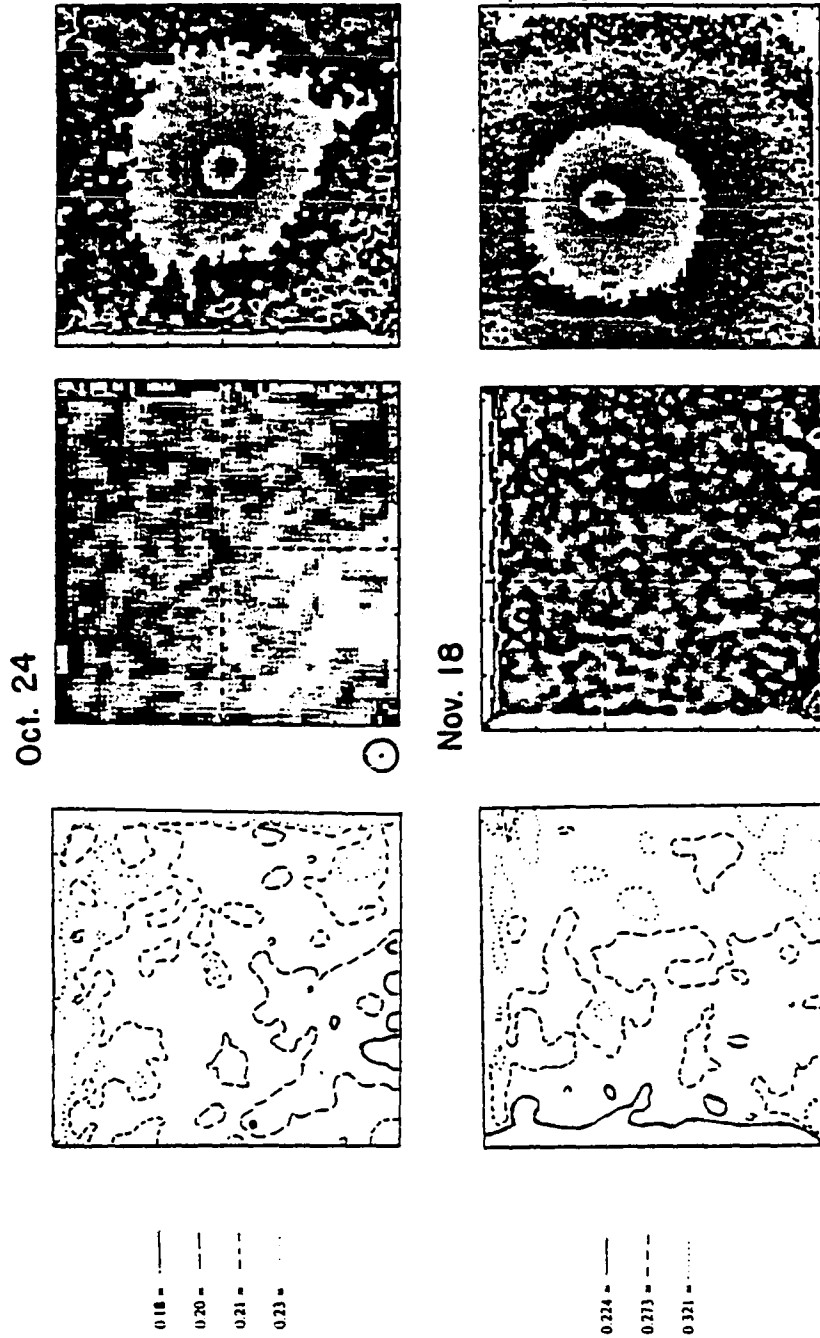


Figure 13--continued

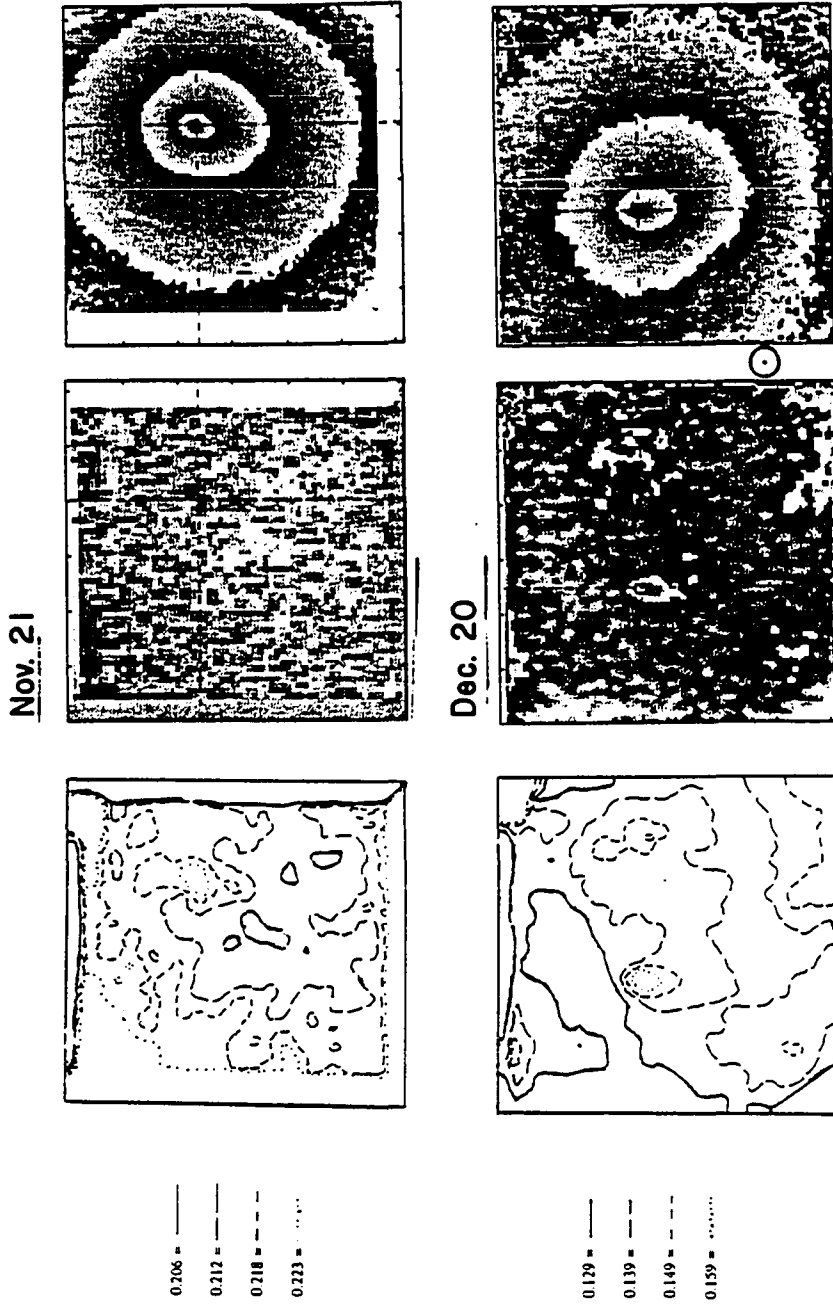


Figure 13--continued

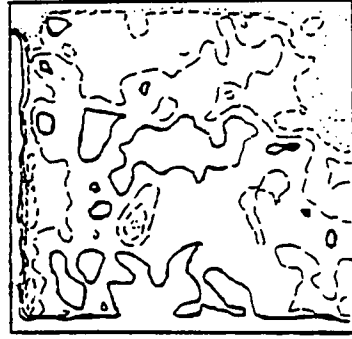
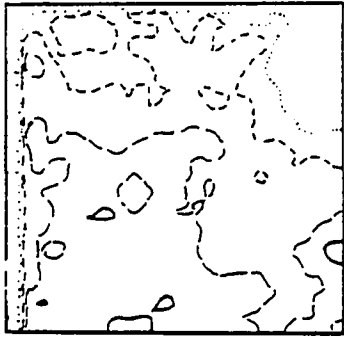
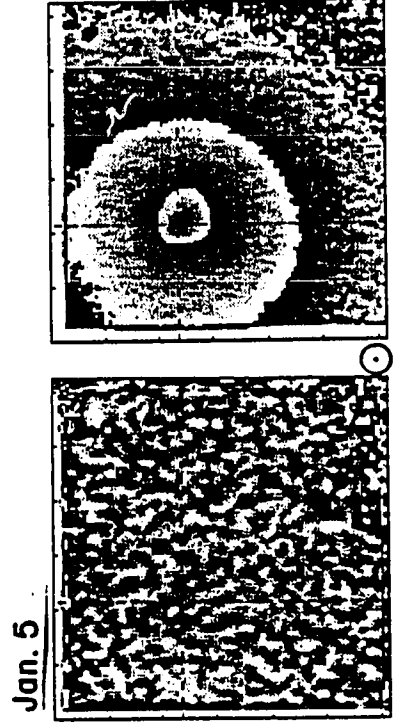
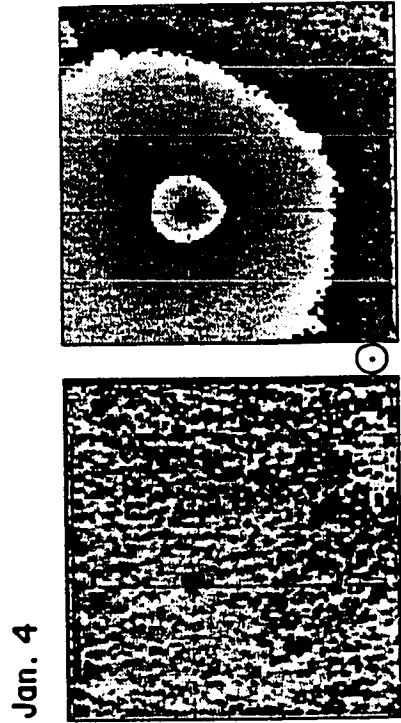
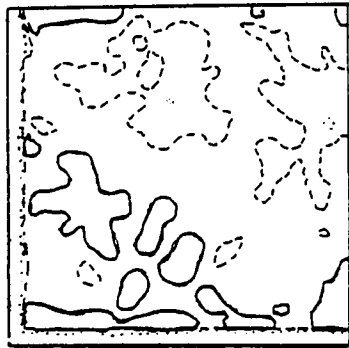
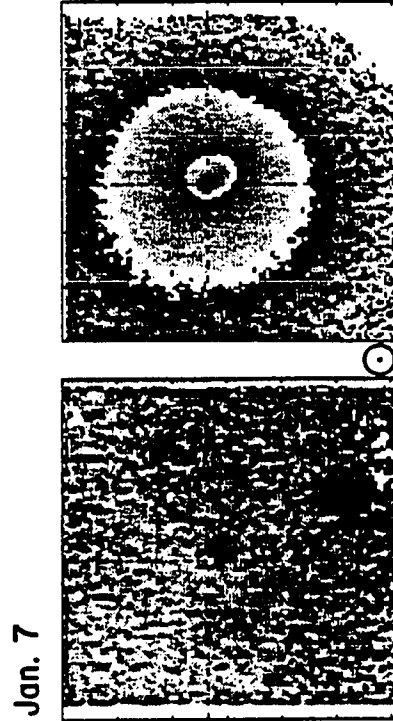
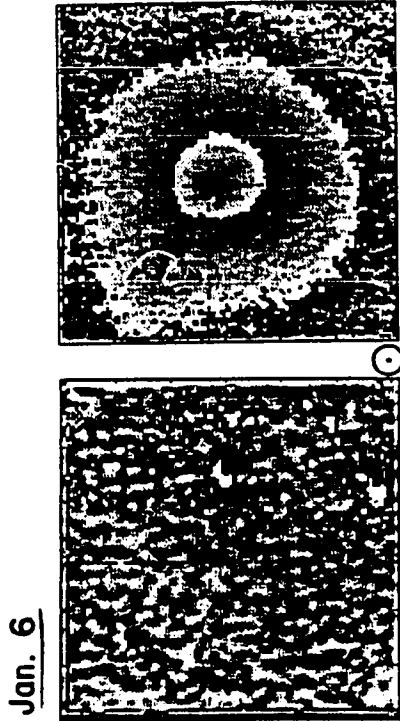


Figure 13--continued



0.150 = ———
0.159 = - - -
0.169 = ·····

0.128 = ———
0.141 = - - -
0.153 = ·····
0.166 = ———
0.179 = - - -
0.192 = ·····

Figure 13--continued

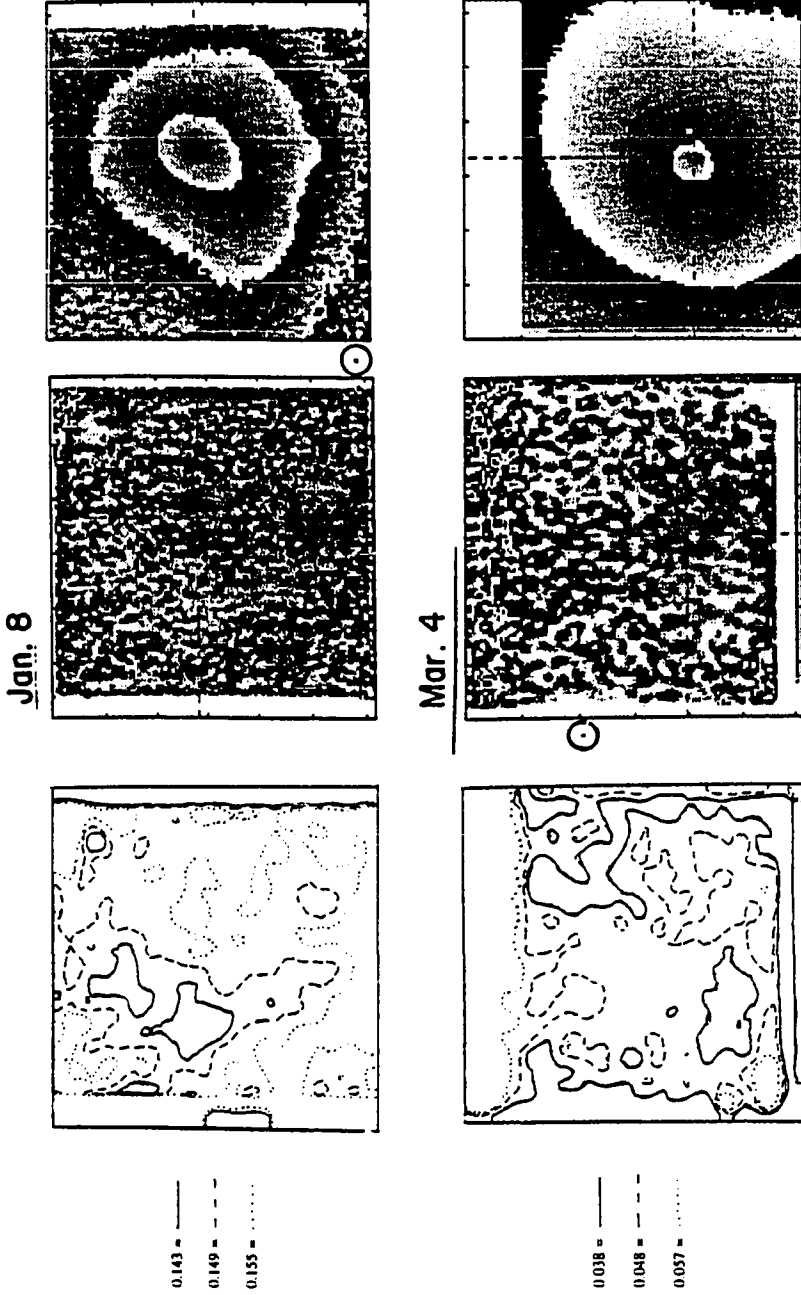


Figure 13—continued

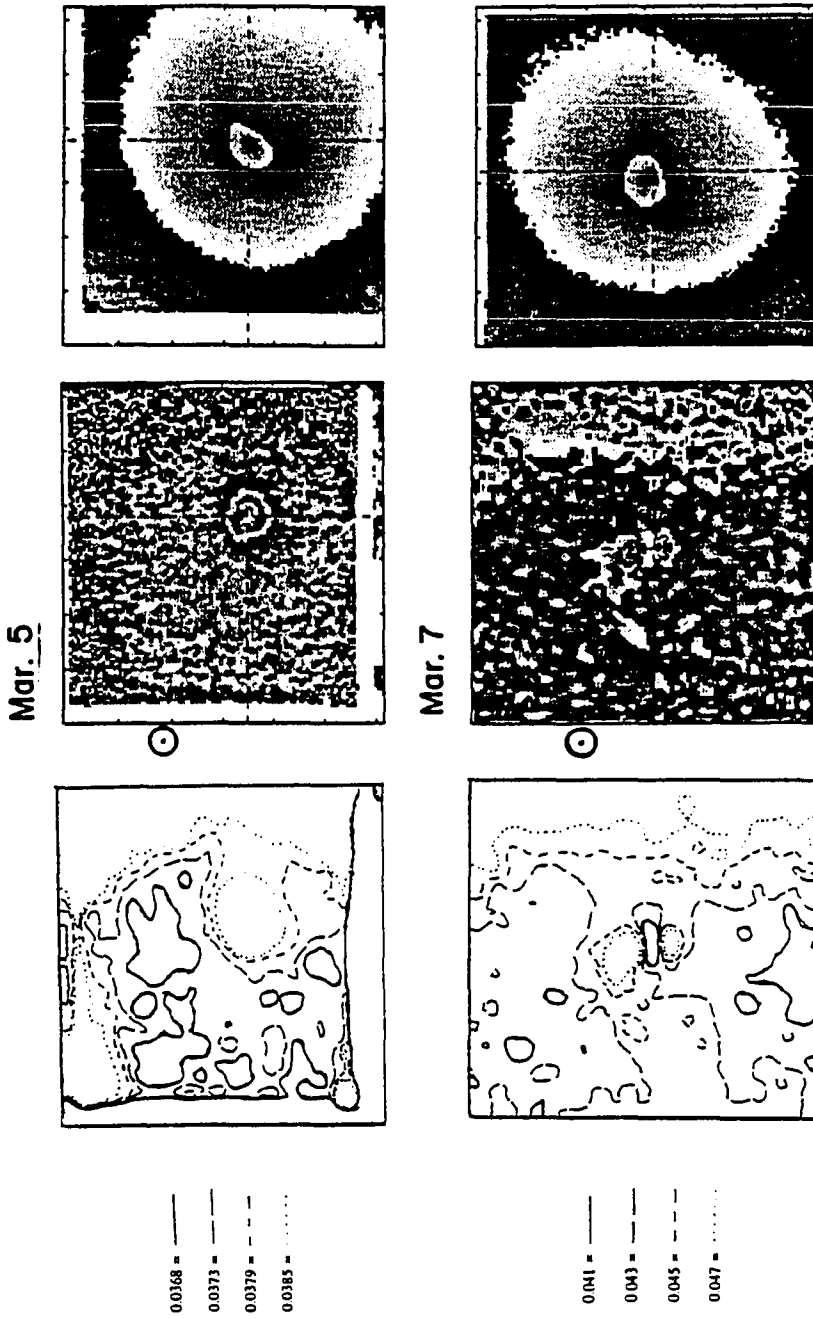
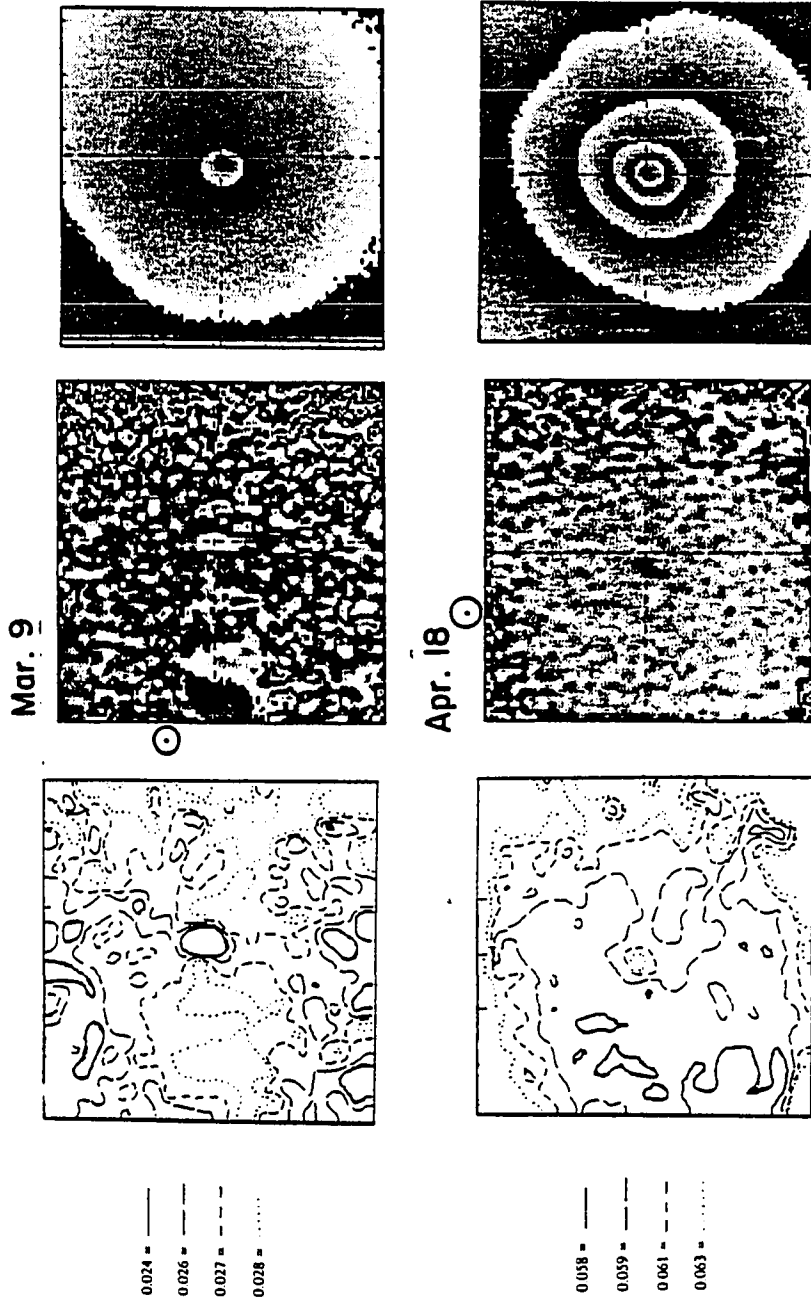


Figure 13--continued



maximum, and never exceed a value of 0.11 until a differential velocities near 20 km/sec are reached.

The observation of differing ratios on each side of the nucleus even at opposition suggests that either the theoretical predictions substantially underestimate the magnitude of the Greenstein effect, or that the outflow velocities in the inner coma are much higher than previously assumed, or that substantial, coordinated bulk motions (e.g., rotation) may be present in the inner coma.

December 20: the sun is to the south-west. The ratio image is lower to the north-east, with values about 0.13, and higher to the south-west, with values of about 0.15. This morphology resembles that predicted by spherically symmetric outflow. There are, however, regions of higher ratio (~ 0.15) to the west and south east of the optocenter, roughly perpendicular to the sunward direction. This ridge could be due to a local peak in the ratio vs. heliocentric velocity curve, that is not seen in Fig. 1. The heliocentric velocity of -26 km/sec puts the predicted ratio at around 0.10, as before, which is slightly below the observed ratio values. These values again suggest a much greater range in outflow velocities than is normally assumed to be present.

January 4: the sun is to the south-west. The ratio image clearly shows higher values to the south-west, of about 0.20, and lower values to the north-east, of about 0.15. The morphology is clearly indicative of spherically symmetric outflow. The heliocentric velocity is still about -26 km/sec, and predicted ratios are about 0.10.

January 5: this night shows much the same morphology. The lower values to the north-east are about 0.12, the higher values to the south-west are about 0.14.

January 6: this night's ratio image has much the same morphology, with lower ratio values of 0.15 to the north-east, and higher values of 0.18 to the south-west.

January 7: again, the sun is to the south-west. The spherically symmetric morphology is much clearer, with the higher values of 0.20 to the south-west, and lower values of 0.13 to the north-east. The greater spread of ratio values may indicate much higher outflow velocities than on previous nights, but as almost all the ratios are well above those predicted, interpretation is difficult. The excess in the OH

(1-1) image (discussed above) is clearly evident.

January 8: the ratio is quite bland. There is some hint of higher ratios to the west and south, and also to the extreme north-east. The higher ratios have values of about 0.17, the lower ratios about 0.14. This might be caused by transient large-scale turbulence in the inner coma, masking the effects of overall gas flow. The continuum image shows very uneven isophotes on this night, that are indicative of strong jets in the inner coma.

The post-perihelion images are not so easily understood. Use of the focal reducer introduced some vignetting, as discussed above. Thus, in general, only the central 60 arcsec square of the images are used in the ratio. There still appears to be some gradient from west to east in the ratio images, due to vignetting by the edge of the filters.

March 4: the sun is now to the north-east. There appear to be higher ratios to the south-west of about 0.06, and lower ratios to the east of about 0.04. These ratios are only apparent within ~30 arcsec of the optocenter, however, with higher ratios appearing again in the northern part of the image. The predicted ratios are at a local minimum of 0.04, which agrees fairly well with the data. The spread in ratio values is indicative of velocities of +/- 4 km/sec, however, which is much higher than usually assumed for the outflow of gas in the inner comae of comets.

March 5: the OH images are very out of focus. The inner 20 arcsec or so of the ratio image are worthless data. Of the rest, there appears to be higher ratios in the antisunward direction, of about 0.038, with the rest of the ratio image showing lower ratios of about 0.035. This spread in ratio values is in excellent agreement with those predicted, and indicates spherically symmetric outflow velocities of about +/- 1 km/sec. The shift in focus would have the effect of washing out the ratio values, however, which might account for their small spread.

March 7: the east-west asymmetry, presumably produced by vignetting, is very noticeable in this ratio image. There is some hint of higher ratios to the extreme north-east, but this is not significant. There is a definite, curved ridge of higher ratios, with values around 0.045, running east-south-east from the central region. The "background" ratio is 0.040. The ridge corresponds to a wide (double?)

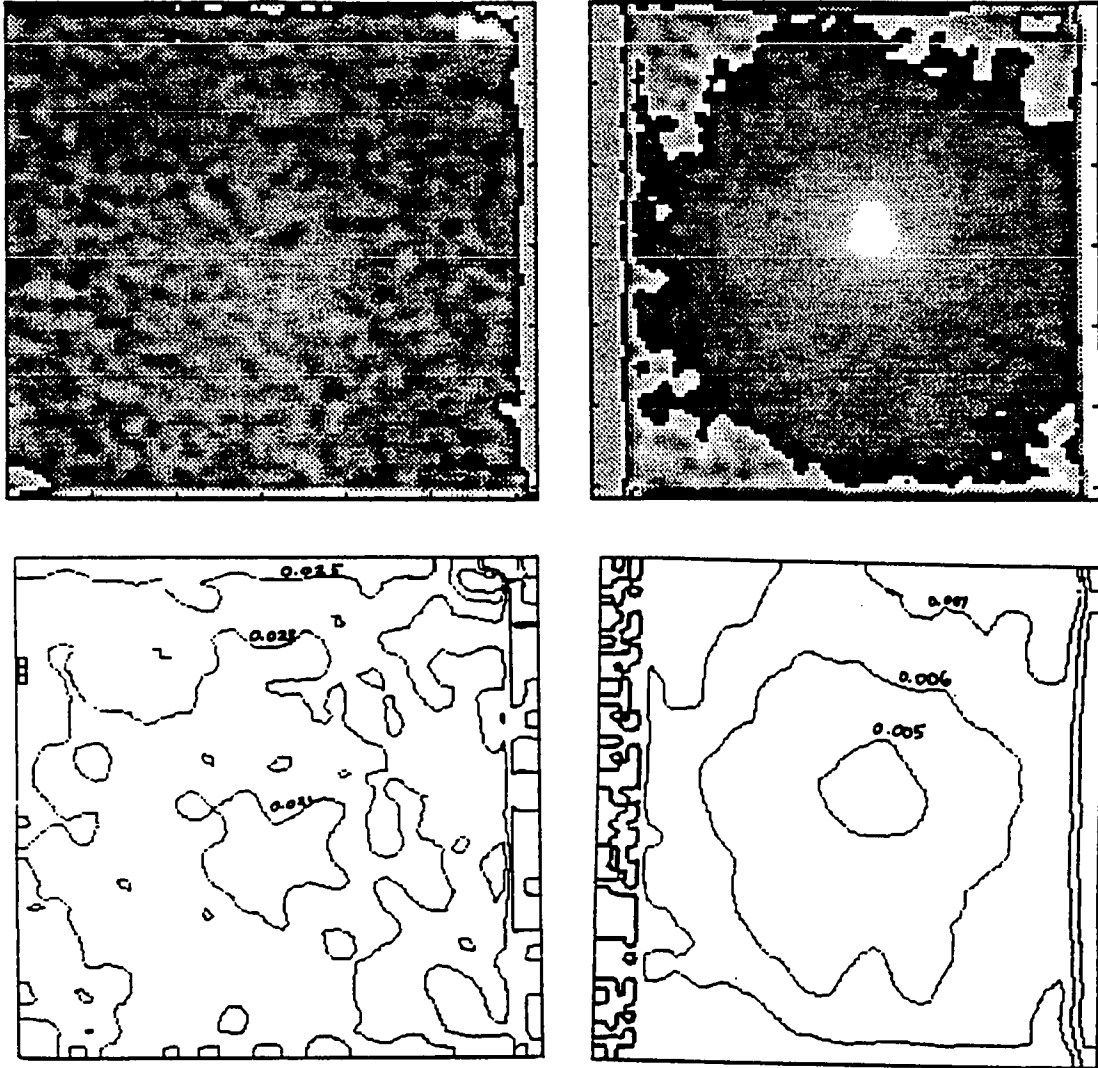
continuum jet in its inner regions, but the ridge in the ratio image is much straighter. The ridge in the ratio image and the jet in the continuum image are not at all coincident towards the edge of the frame. This jet would have a velocity about 3 km/sec higher than the surrounding gas, according to the predictions of Schleicher and A'Hearn. The east-west asymmetry referred to earlier prevents any detailed analysis of the morphology of the outflow of the background gas. Note that the gas "jet" does not coincide with any flat-field feature.

March 9: again, the ratio image is chaotic. The sun is (still) in the north-east, but the ratio image shows lower areas, of about 0.023, to the north and south, with a ridge of higher ratios, of about 0.03, running east-west through the optocenter. The continuum image on this night showed a broad sunward fan, with a weak jet to the west. The ridge in the ratio image could correspond to OH from the source regions of these continuum features, superimposed on a turbulent background. The ridge does not line up across the sunward direction, and the ratio image cannot therefore be explained by spherically symmetric outflow, at a minimum in the ratio vs. heliocentric velocity graph.

April 18: the comet is near opposition, although the phase angle is 30 degrees. The sun is to the north-north-east. The ratio image shows lower values to the southeast, of about 0.058, and higher values opposite that, of about 0.063. The overall velocity of the comet (+26 km/sec) puts it right at a local minimum in the ratio vs. heliocentric velocity plot. The only way to explain the observed ratios is if the comet's overall heliocentric velocity is really +30 km/sec, and the outflow is at +/- 4 km/sec. Both values are much higher than calculated for the comet at this time. Alternatively, the gas in the inner coma could be rotating, with average velocities of +/- 4 km/sec along the LOS.

The 1σ error the ratio images is shown in Fig. 14, for a typical night (January 8), and the night with the weakest signal (October 24). These images were obtained by a simple propagation of errors method, taking into account noise in the OH band images. Also shown are conventional contour plots of these error images. Errors in the extinction and continuum correction were much smaller. The continuum band image did not contribute significantly to the noise in the ratio, due to the large flux in that band. Note that the error gets larger, further from the optocenter. This is a straightforward consequence

Figure 14--Error Images and Contour Plots



of the signal getting weaker, and therefore the signal-to-noise (S/N) becoming smaller, farther from the optocenter. Although the error in October is about five times that in January, the ratio image still has an S/N of greater than 10 in the central region. I would therefore conclude that the calculated ratios are good to at least 10% on all nights.

CONCLUSIONS

Spherically symmetric outflow dominated the morphology of the gas flow in the inner coma pre-perihelion, but some turbulence and nonuniformities (jets?) are apparent post-perihelion. The pre-perihelion ratio values do not agree very well with the predictions of Schleicher and A'Hearn (1982). While the post-perihelion ratios are closer to those predicted, the spread in the ratios is much wider, and indicates a range of gas outflow velocities generally four times that normally observed in comets. Simple propagation of errors (Fig. 14) shows that the observed ratios are accurate to at least 10%. The quantitative difference between the observations and theory is real, and implies much higher gas outflow velocities than previously observed (Krankowsky et al. 1986, Larson et al. 1986). The solar spectrum used in the calculations by Schleicher and A'Hearn (1982) may not correspond to the spectrum of the sun at the time of the observations. It is possible that the theoretical calculations of the magnitude of this effect are in error, with large fluctuations in the ratio on a much finer heliocentric velocity scale than that used for the calculations.

The Giotto spacecraft measured the measured an expansion velocity of 0.9 ± 0.2 km/sec for H_2O in Halley in March (Krankowsky et al. 1986). This measurement was based on the shift of the 18 amu (water) peak in the neutral mass spectrometer. The authors state that, in making this measurement, "a very careful data reduction and comparison with calibration data is necessary". Ground-based measurements of the width of H_2O lines (Larson et al. 1986) gave velocities of 0.9 ± 0.2 km/sec pre-perihelion, and 1.4 ± 0.2 km/sec postperihelion. The OH molecules should have a higher velocity dispersion than the water molecules from which they are formed (Festou 1981). This dispersion in velocities is not likely to be on the order of 2-3 km/sec, however, and therefore probably will not account for the higher ratios seen in this work.

Many observers report anisotropies in the gas distribution in the coma of Halley's comet. Larson et al. (1986) and Weaver et al. (1986) see sunward-antisunward asymmetries in their ground-based observations of H₂O. Hsieh et al. (1987) note a difference between the gas density encountered before and after closest approach of the VEGA flybys. The cyanogen jets previously referred to (A'Hearn et al. 1986, 1987) are gaseous asymmetries, but are probably evolved from dust in the coma, and are not necessarily indicative of any non-uniformity in gas production from the nucleus. Most of these non-uniformities are on a scale much larger than that covered by the OH observations presented here.

Excess emission at the optocenter of the OH (1-1) band images was repeatedly observed. Following the suggestion of Bertaux (1985), this excess is explained as emission from high level states in the OH (0-0) band, which are populated only through the breakup of water into H and OH. The radiative decay of these states results in excess flux in the (1-1) band images, only in those regions where water is being broken down. A detailed analysis of this effect is difficult, due to the guiding errors in much of this data. Figure 12 shows data from January 7, when the guiding was good and the excess present. It is a (1-1) band image with the continuum removed, and the corresponding (0-0) band image scaled to match the wings of the (1-1) band image, and then subtracted off. Figure 12 should consist of light from only those lines of sight containing regions where water is being broken down into H and OH. The overall north-east/south-west asymmetry evident in the image is a manifestation of the Greenstein effect. The peak in the middle is similar in appearance to a point source, except for a slight sunward projection. This projection looks like a similar projection in the continuum image, and may be the result of a slight error in the continuum removal.

Observations of cometary OH made in this manner are good indicators of cometary activity. Deviations from spherically symmetric outflow, when present, are very obvious. The existence of an "OH1 excess" is a sensitive guide to the H₂O production rate. If the data and the theory can be made to correspond better, then a more quantitative interpretation of the gas flow would be possible. At the present state of understanding, these results are useful primarily for the qualitative interpretation of the morphology of gas flows in cometary comae.

CHAPTER 4

SUMMARY

Chapter 2 detailed the investigation of filamentary sublimate residue (FSR). Powdered mineral samples were mixed with liquid water and flash-frozen, and the ice sublimed away in a vacuum. Some types of mineral particles were observed to cling together and form a low density, highly insulating material (FSR), after the water was gone. It was found that, of all the major classes of silicate minerals, only the phyllosilicates formed FSR. Of the phyllosilicates, only species with significant amounts of interlayer water were reduced to smaller crystalline units ("tactoids") and rebonded into FSR. These FSR forming minerals were smectite clays, closely related vermiculite, and the hydrated mica illite. Common meteoritic minerals such as olivine, pyroxene, feldspar, and serpentine did not form FSR, although small amounts of FSR forming minerals could bind significant amounts of non-FSR-forming material together.

The FSR forming process was better defined in chapter 2, than it previously was by Saunders et al. (1984). The presence of interlayer water in the mineral tactoids allows them to keep a semiliquid layer around them, even when imbedded in a frozen matrix. When two tactoids come into contact, this surface layer of water allows them to coordinate their crystal structures to a certain extent, and bond together into a single unit of the original material. This accounts for the high tensile strength of the FSR, as well as its high electrical conductivity. Electrostatically bound agglomerations would not drain off charge in a scanning electron microscope (as FSR was observed to do) without being coated by a conducting layer.

A further part of the investigation studied the effects of organic materials on the formation of FSR. The presence of organic tar in the simulation did not inhibit the formation of FSR in minerals that formed FSR of their own accord. Further, the tar would bind together minerals that did not form FSR into a very strong, FSR-like substance, even when present as only a small proportion of the total solid

mixture. The FSR so formed tended to be much denser, with fewer, larger pores than the pure mineral FSR. It was significantly stronger, as well. The presence of organic materials in comets is fairly well demonstrated by their presence in Brownlee particles, as well as the "CHON" particles observed in P/Halley by the spacecraft flybys.

Chapter 2 demonstrated that it is quite possible that dust particles cling together to form refractory mantles in comets and (possibly) in Martian polar layered terrain. These mantles have very low densities, high porosities, and low thermal conductivities, making them excellent insulators. It is quite possible to store large amounts of volatile material under global disequilibrium situations, when they are covered by comparatively insignificant amounts of FSR.

Chapter 3 investigated the gas flow morphology and velocity in the inner coma of Halley's comet. The main result is the observation of non-uniform outflow from the nucleus. While most observations showed a spherically symmetric outflow morphology, some observations (made right after perihelion passage) showed unmistakable jets in the inner coma. Great care would have to be taken in interpreting spectra made while one of these gas jets was present.

The dissociation of water into H and OH radicals was also observed. An image of the region where the water was dissociating was made for the first time. This image confirmed that the dissociation region is small, although possibly asymmetric. The comet was too far away, and the guiding errors and the effects of smoothing during data reduction too great, to allow any more detailed interpretation of this data.

Chapter 3 demonstrated that this technique of observing the Greenstein effect is feasible, although agreement with theory (Schleicher and A'Hearn 1982) was poor. It is suggested that large variations in the OH band ratio exist, on a much finer velocity scale than that used in the calculations of Schleicher and A'Hearn, or that the solar spectrum used in their calculations differed from the actual spectrum at the time of the observations. The extremely high relative velocities suggested by direct comparison of the data with the theory are not borne out by other observations (Larson et al. 1986, Krasnopolsky et al. 1987).

The extinction in the extreme (ground-based) ultraviolet (UV) region of the spectrum was also measured to a high degree of accuracy, showing a low extinction value and high linearity of extinction with airmass, in the filter bandpasses used. The sky contribution to the data was demonstrated to be negligible, confirming observations of purely photometric observers (D.J.Tholen, pvt.comm.). Finally, problems in flat-fielding images made with the Galileo/IfA CCD were overcome, showing the necessity of matching the color of the flat field source to that of the object observed.

The two main results of this work are the demonstration of significant binding forces between small mineral grains in volatile environments, and the observation of occasional non-symmetric outflow of gas in cometary comae.

Further work can be done in both areas. The simulations have, for the most part, been done only once, so the experiments need to be repeated to confirm the results. More work is necessary to study the types of organic materials that bind minerals together, and to measure quantitatively how well the FSR so formed is bound. Systematic observations of outflow morphologies in comae of other comets need to be conducted, to see if non-uniform outflow is a common cometary phenomenon. It is quite possible that P/Halley is a unique case.

APPENDIX

OBSERVATIONAL PROCEDURES

Images were obtained with the Galileo/IfA charge-coupled device (CCD) (Hlivak et al. 1982) at the cassegrain focus of the U. Hawaii 2.24m telescope at Mauna Kea Observatory. Two custom made filters isolated the OH (0-0) and (1-1) transitions around 3100 Å, and a third isolated the nearby continuum, around 3700 Å (6840 Å postperihelion). An f/4.5 focal reducer was used post-perihelion. Bias level subtraction was done in the usual manner for the CCD, by subtracting the mean extended register value from the image. Flat fields were obtained by imaging the bright dawn or dusk sky ("sky flats"). Bad columns in the images were removed in the usual manner, by linear interpolation of the adjacent columns. Cosmic ray strikes were removed by a special program that sets both the high pixel and its neighboring pixels to the average value of the 16 pixels immediately adjacent to that area. The optocenters of the images were located to within a tenth of a pixel by the least-squares fitting of a gaussian to the central peak. The images were aligned by adding appropriate numbers of rows and columns, and then using linear interpolation to shift the fractional part. The images were multiplied by the appropriate factor to correct for atmospheric absorption. This factor was found by nightly determination of the extinction coefficients, and the mean airmass at which each image was made. The images were smoothed to remove the pixel to pixel variations caused by the read noise in the CCD. "Bad" spots not removed by the cosmic ray removal process or the bad column removal process were removed interactively, by a cubic spline fit to an annulus surrounding the spot in question. Finally, the contamination of the OH images by sky light and continuum was removed, resulting in images made only in the light of the (0-0) and (1-1) transitions of the hydroxyl radical. The (1-1) image was then divided by the (0-0) image, to give an image of the gas flow velocity in the sunward direction, averaged along the line of sight.

IMAGE ACQUISITION

Profiles of the filters used are shown in Fig. 15, along with a schematic of the OH bands investigated (Lane et al. 1974). The filters were blocked to less than $10e-4$ transmission to a wavelength of $1.1 \mu\text{m}$. Transmission curves measured before and after the observing season showed no detectable change in the filter curves, and no change in the (lack of) transmission out to 9000 Å. Standard stars were observed through the filters with and without a piece of (uv-opaque) glass. With the glass in place, the standard stars were not visible. These observations confirm the absence of red leaks in the filters, at least to the cut-off wavelength limit of the CCD.

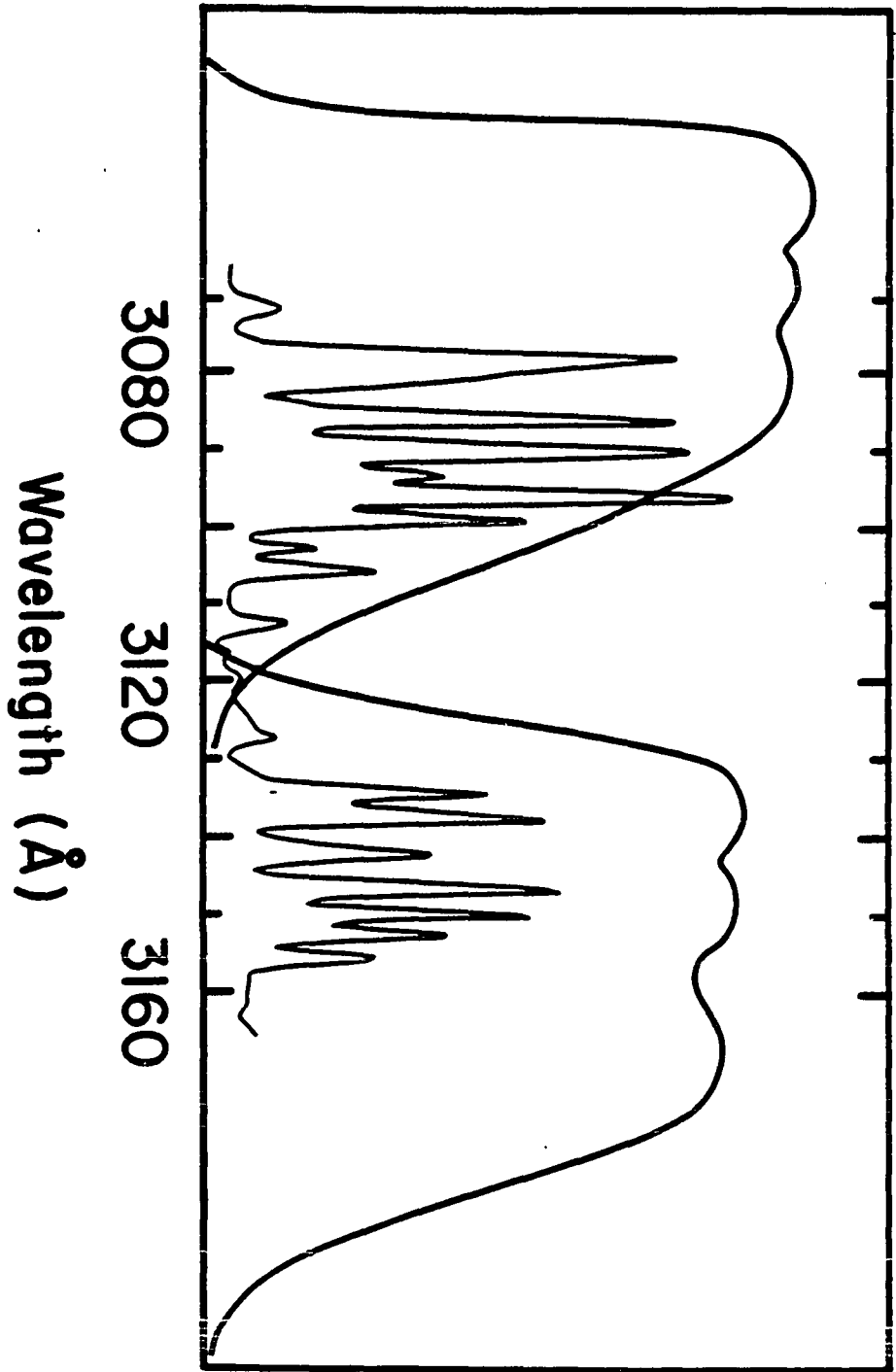
Table 4 lists the nights that OH data was obtained, and the filters used, as well as some comments. All exposures were made with cometary tracking rates set into the guiding computer, due to a lack of on-axis guiding capability at the 2.24m telescope. Telescope flexure caused some guiding problems, but these could be corrected for in longer exposures by changing the tracking rates as if correcting for refraction. The central peaks were trailed by 2-3 arcsec over a 10 min exposure at ~ 2 airmasses, although markedly better (and worse) results were obtained (Table 4). Each pixel was 0.28" across in preperihelion images, and 0.54" across, postperihelion.

The addition of an $f/4.5$ uv-transmitting focal reducer for the post-perihelion observations was a mixed blessing. The field of view effectively doubled in size, but the edge of the filter came into view. This is due to the fact that the CCD, in its normal mounting position, is not exactly on the optical axis of the telescope. The focal reducer also made the focus much more delicate. Note that on-chip binning was used in recording the data, so that the raw images were 250x250 pixels.

BASIC IMAGE REDUCTION

All image processing was performed at the Institute for Astronomy's image processing facility, on the Perkin-Elmer 3660 system, or the VAX 11-780 system, running the "Zodiac" processing routines. The canonical image reduction procedure is described in Heasley et al., 1984.

Figure 15--Filter Profiles



Bias subtraction was accomplished in the usual manner. The rightmost 8 columns of the Galileo/IfA CCD are covered--never exposed. This is called the extended register. The average value of the extended register is subtracted from the image to correct for bias induced by the data system.

Major problems were encountered in using the standard flat-field techniques, and thus flat-fielding will be discussed separately.

There are 16 bad columns in the Galileo/IfA CCD which were removed by linear interpolation of the adjacent data. This works quite well for single bad columns, but leaves something to be desired in the cluster of 3 bad columns (in 2x2 binning mode) toward the right edge of the chip. These bad columns show up as rows, near the bottom of the image pre-perihelion, and near the top post-perihelion, when rotated to the sky orientation (north to the top, west to the right). Linear features in these regions are probably spurious.

Cosmic ray strikes were removed by a special routine that detects large pixel to pixel variations. Most cosmic ray strikes have a "skirt" of pixels significantly higher than the surrounding data. The routine therefore sets the aberrant pixel and its neighbors to the average value of the 16 pixels immediately around them. The routine has a problem of trying to "correct" sharp peaks in the data (e.g., the optocenter of the continuum images), so the routine was not applied to the central 20 pixel (~5 arcsec) square region around the peak of each image.

A few blemishes in the chip were not removed by these processes. These were dealt with on an individual basis by an interactive routine which will be discussed later.

The position of the optocenter of the images was determined by fitting a gaussian profile to the peak of the images. The central position was calculated to be good to at least 0.01 pixel. The images were then aligned by adding the necessary numbers of rows and columns, and by linear interpolation to shift the image by the fractional part. The slight smoothing induced in this procedure was much smaller than the smoothing done later, to reduce the pixel to pixel noise. The alignment was adjusted in the last step, ratioing, to give the most even fit possible. The assumption was made that the optocenters of all the images (gas and continuum) line up. To the accuracy of the guiding, this is correct.

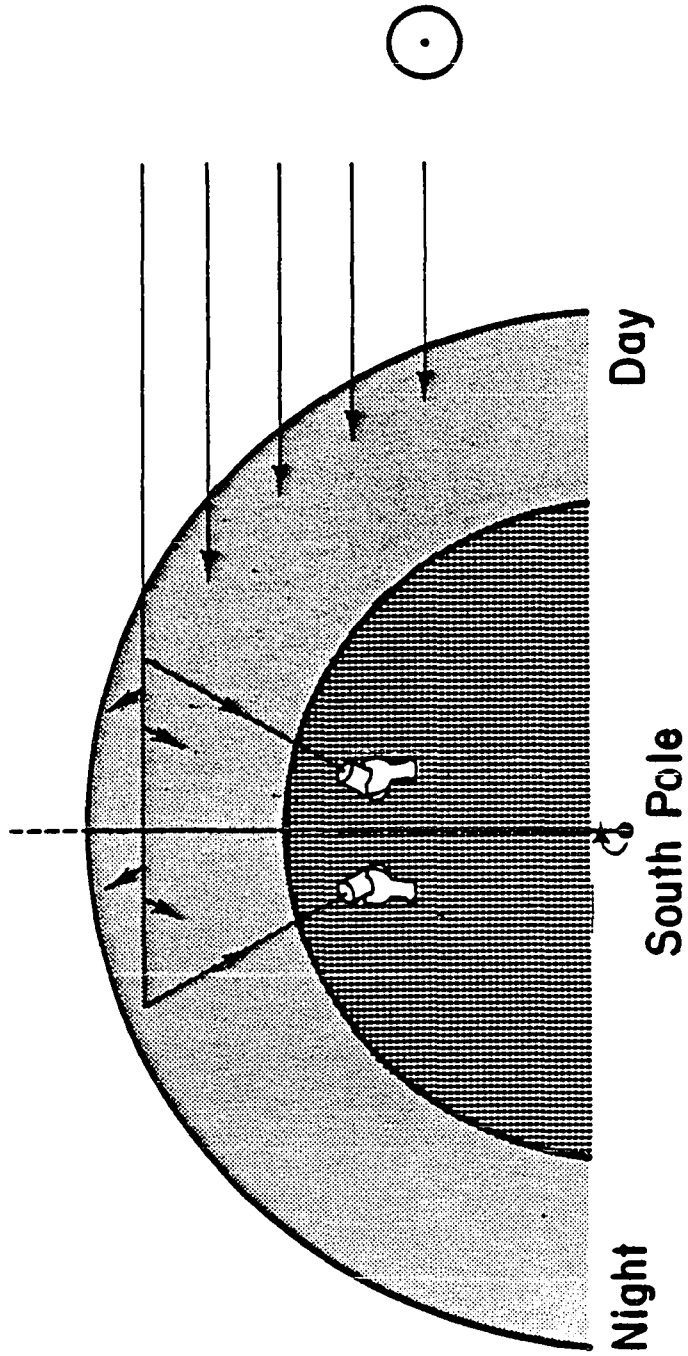
FLAT FIELDING

The major difficulty encountered when reducing these images was the correction for irregular sensitivity across the CCD. The usual method for correcting for these variations is to make several images of the (closed) dome slit, which is illuminated by a floodlight. The floodlights used in this method produce almost no flux in the UV, however, so images of the dawn or dusk sky, made with the telescope at the zenith, were used to obtain flat fields with reasonable flux.

The images of the comet over-filled the field of view, with the data numbers at the edge of the frame being a considerable fraction of those in the peak. In addition, at least for the OH bands, there were no distinct features in the images. This work therefore provides some of the most stringent tests for flat-fielding technique yet made. Small errors in the flat-fielding process, which might have gone unnoticed in images with large contrast and/or low signal (sky) areas, show up clearly in these cometary images. In addition, few attempts have been made to use the CCD in the UV, and certainly none at this extreme wavelength. M. Pierce (pvt. comm.) reports some problems "on the 10% level" in flat-fielding Johnson U-band images of galaxies, but most of these problems would occur in low-signal sky regions, where careful assessment of the flat-field's accuracy would be difficult. Standard flat-field techniques are not useful in the UV.

For a flat-field to work well, the color of the illuminating source must resemble the color of the object in the image. Thus, the "red" flat fields obtained off the dome slit covers do not flatten pictures of a comet which has a more uniform, "white" color. It was found that sky flats made while the sun was below the horizon (but while the sky was quite bright) did not work well either. The reason for this is shown in Fig. 16. Just on the night side of the terminator, the telescope (pointing at the zenith) is looking at scattered light that has travelled through a considerable stretch of atmosphere, and has had most of the blue light removed by Rayleigh scattering. Just on the day side of the terminator, the sunlight is scattered into the telescope without having so much of the UV light removed, and thus the color is more neutral than red. This results in a much better flat field for the cometary images. Exposure times for the flat fields drop dramatically, depending on whether or not the sun is above the horizon: a

Figure 16--Flat Field Observational Geometry



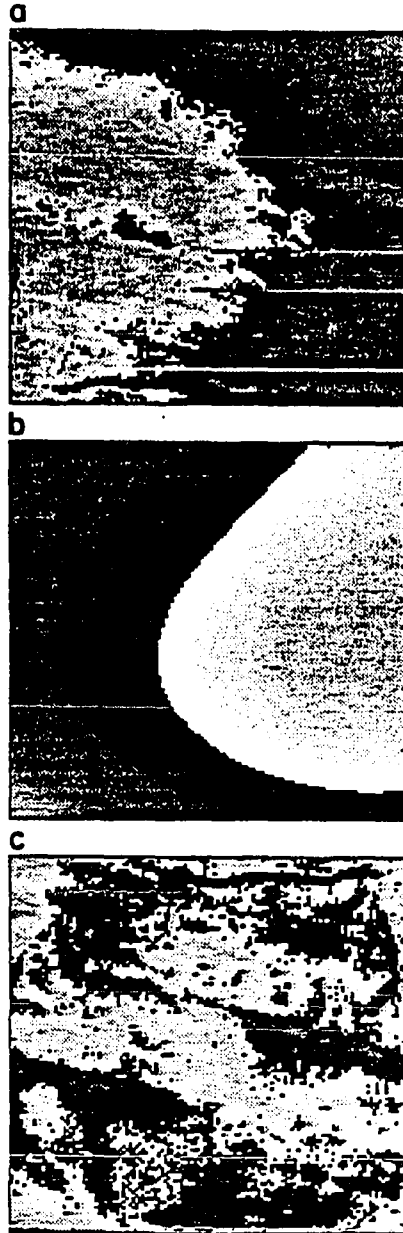
difference of even a minute can be noticed. This change in exposure time corresponds to a change in UV flux from the sky around sunrise.

Only post-perihelion flat-fields were made with the sun above the horizon. These flat-fields worked quite well with the standard flat-field processing technique on the data for these runs. Problems were encountered in applying these flats to the pre-perihelion data, however, due to the vignetting induced by the focal reducer used post-perihelion. A compromise was made by fitting a two dimensional quadratic surface to the March flat fields, and dividing the flat fields by this surface. The quadratic fit is shown in fig. 17, along with the flat field before and after division. This altered flat worked quite well for the pre-perihelion images, with only features with a very low spatial frequency (less than 1 cycle per image) remaining in the flattened images. The same flat fields worked for OH (0-0) as well as OH (1-1) images, so any low spatial frequency differences due to flat-fielding should disappear in the ratio, anyway. High frequency differences might remain, due to the offset necessary to align the images for ratioing.

EXTINCTION CORRECTION

Standard stars were selected each night from the International Halley Watch (IHW) standard star list. A red and a blue star were observed at as wide a range of airmasses as possible. These observations determined the extinction coefficient on each night. The mean airmass for the exposure was used, because exposure times ranged up to several minutes for faint red stars at high airmasses. The mean airmass varied from the mid exposure airmass by a few percent at most. Flat-fielding standard star measurements had no effect on the measured flux value above the few percent level, so the flat fields used were irrelevant to the determination of the extinction coefficient. (The images of the standard stars were made on the same area of the CCD chip). Fluxes from the stars and the adjacent sky were measured with a box photometry program. The box size was selected to cover over four times the area that a star was visible in its image frame, and the corresponding sky value determined in an unvignetted portion of the sky part of the image frame. The sky values were found to be essentially zero in all filters, well below the noise induced by the CCD read-out electronics. This low sky value is consistent with the

Figure 17--Flat Fields and Correction Surface



photometric observation (D. Tholen, pvt. comm.) that the sky values in the IHW OH filter were orders of magnitude smaller than those sky values observed in any other filter.

The color terms determined in the standard manner were negligible for observations made below 3 airmasses, and were thus ignored in the data reduction. The extinction coefficients were determined for a least-squares fit to a plot of $2.5\log(\text{counts})$ against mean airmass (fig. 18). The results are given in Table 5. Average values for the extinction coefficient were used on nights when not enough standard star observations were made (early in the observing sequence, it was not apparent that such care was necessary). The images were corrected by multiplying by:

$$C = 10^{\frac{\Delta m}{2.5}} \quad (1)$$

where $\Delta m = kX$, k = extinction coefficient, X = mean airmass of observation. Note (from Table 5), that the coefficients for blue stars are much more self-consistent than those for red stars. This is probably due to the greater apparent brightness (in general) of the blue stars, and therefore the shorter exposure time necessary to measure them, as well as the higher number of counts obtained per measurement. The coefficients from blue stars were used to correct the observations.

Figure 18 shows some typical plots of magnitude vs. airmass, and the lines fitted to the data to measure the extinction coefficient k . Note that the extinction at 3000 A was linear to 3 airmasses on most nights. All cometary observations were made at airmasses at which the extinction coefficient was linear, so no further processing of the data was necessary to correct for the effects of the Earth's atmosphere.

Cometary observations were generally made at very different times from the standard star observations, and might therefore have very different amounts of sky contamination. The observations of January and March, in particular, were made during astronomical twilight. A system was devised to correct for this unknown and variable sky brightness. The assumption was made that the brightness in the ratio images did not vary significantly in the radial direction. This assumption is justified by the observation that the OH images were featureless, having only very large-scale structure. An average profile of each OH image was obtained by finding the mean of the data values in concentric annuli,

Figure 18--Extinction Curves

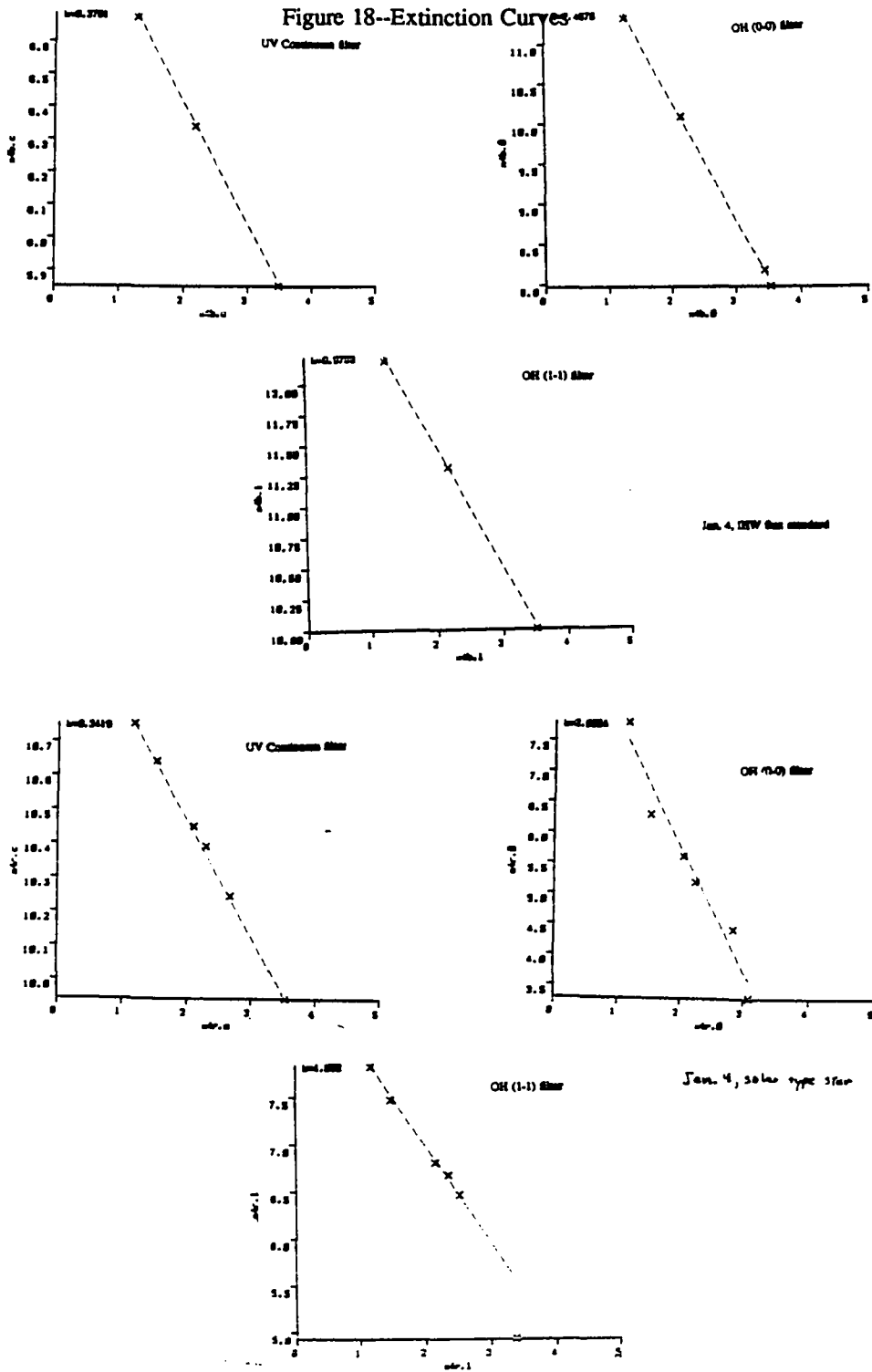
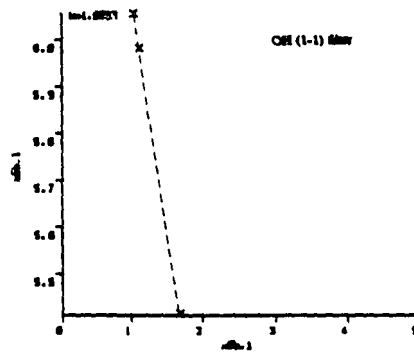
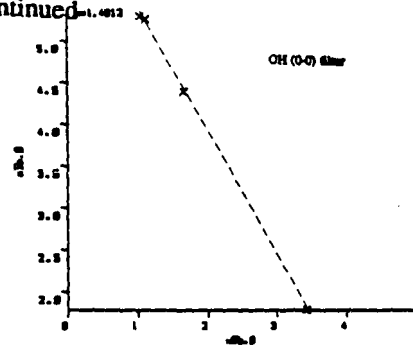
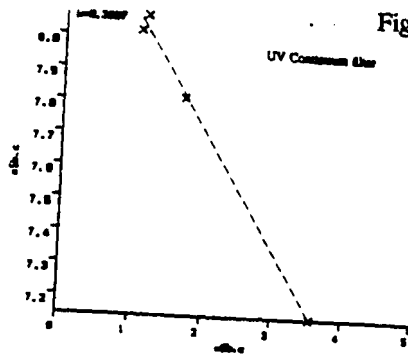
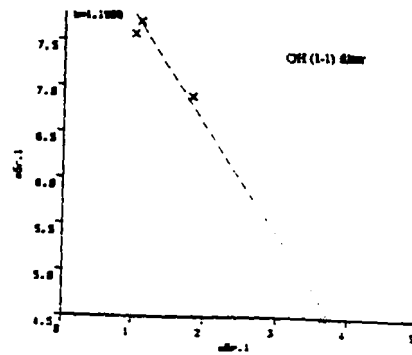
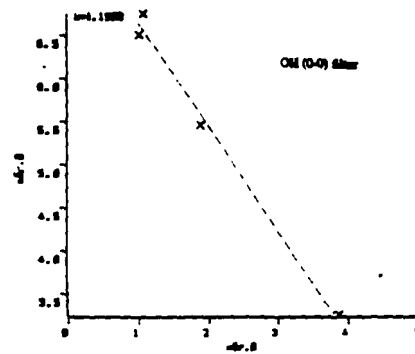
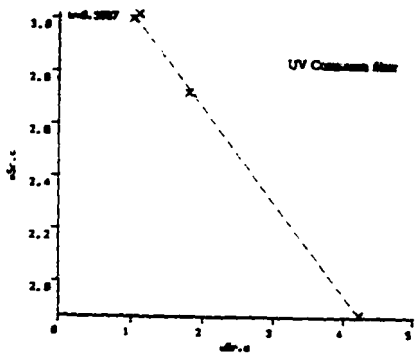


Figure 18-continued



Jan. 2, IRW film standard



Jan. 5, anti-cyan star

Table 5

EXTINCTION COEFFICIENT SUMMARY

DATE:	RC	FLUX STANDARD			NUMBER
		UVC	OH1	OH0	
12/20	-	0.3755 (.003)	1.5834 (.078)	1.3540 (.031)	4
1/4	-	0.3701 (.002)	0.9759 (.016)	1.4575 (.029)	3
1/5	-	0.3607 (.019)	1.0093 (.007)	1.4812 (.023)	4
1/6	0.0922 (.003)	0.4134 (.003)	1.0193 (.033)	1.5155 (-)	3
1/7	0.0492 (-)	0.3815 (.004)	0.9417 (.005)	1.4392 (.055)	3
1/8	0.0658 (.007)	0.4146 (.032)	0.7230 (.164)	0.5334 (.317)	3
3/4	0.0376 (.011)	-	0.9153 (.011)	1.5510 (.009)	3
3/5	0.1008 (.033)	-	0.9173 (.006)	1.4654 (.011)	6
3/7	0.0512 (.007)	-	0.9141 (.004)	1.4164 (.075)	5
3/9	0.0505 (.004)	-	0.9290 (.017)	1.4752 (.018)	5

(errors in fit in parenthesis)

good points have errors less than 10%

- means no data

(-) means only 2 stars determine the coefficient

EXTINCTION COEFFICIENT SUMMARY CONTINUED

DATE:	SOLAR TYPE STAR				NUMBER
	RC	UVC	OH1	OH0	
11/18	0.784 (.025)	0.2629 (.120)	0.9881 (.005)	1.4020 (.156)	3
12/20	0.0401 (.001)	0.4024 (.011)	0.9660 (.033)	1.5146 (.005)	5
1/4	-	0.3419 (.005)	1.2590 (.117)	2.0554 (.210)	3
1/5	-	0.3557 (.011)	1.1969 (.077)	1.190 (.081)	4
1/6	-	-0.394 (-)	0.9688 (.026)	1.5598 (-)	2
1/7	0.0142 (-)	0.3935 (.007)	0.9861 (.043)	1.3638 (.207)	4
1/8	-	0.3696 (.007)	1.0268 (.003)	1.4315 (.031)	4
3/4	0.8290 (-)	-	0.9877 (.006)	1.4307 (.008)	3
3/5	0.0623 (.008)	-	0.9031 (.015)	1.5975 (.042)	6
3/7	0.0607 (0.11)	-	0.9413 (.015)	1.4084 (.057)	6
3/9	0.0573 (.006)	-	0.9403 (.015)	1.6082 (.057)	6

AVERAGE: (IHW Flux Standard)

	RC	UVC	OH1	OH0
all pts	0.0657	0.3684	0.9929	1.4558
gd. pts	0.0640	0.3860	1.0199	1.4617

AVERAGE: (Solar Type Star)

	RC	UVC	OH1	OH0
all pts	0.1631	0.3598	0.9748	1.5056
gd. pts	0.0401	0.3759	1.0133	1.4760

used: 0.055 0.370 1.015 1.470
(values for nights with no data)

from the optocenter to the edge of the image. The behavior of the outer portions of the ratios of the OH (1-1) to the (0-0) profiles was determined by the amount of skylight present. If the ratio image profile turned up toward the edges, the OH (1-1) image had sky contamination: the (1-1) image was acting more as a constant and the ratio profile was approximately the inverse of the OH (0-0) image profile. If the ratio turned down at the edge, the OH (0-0) image had sky contamination: now, the (0-0) image was acting as a constant and the ratio profile resembled that of the OH (1-1) image. The strength of the sky contamination was determined by subtracting different values from the OH band images, and observing the behavior of their subsequent ratio. This correction was checked by making several ratios of the images, with slightly different sky values used, to confirm that the sky subtraction was adequate.

It can be demonstrated that this process eliminates all sky contamination. If A is the flux in a pixel in the (1-1) band image with sky flux C_1 , and B is the flux in a pixel in the (0-0) band image with sky flux C_2 , then after processing in the above manner, we know that at two positions in the images (at the same azimuth),

$$\frac{A_1+C_1}{B_1+C_2} = \frac{A_2+C_1}{B_2+C_2} \quad (2)$$

This may be solved for C_1 :

$$C_1 = \frac{A_2B_1 - A_1B_2 + C_2(A_2 - A_1)}{B_2 - B_1} \quad (3)$$

If the flux falls off with distance x from the optocenter in the same manner in each band (e.g., exponential, power law, etc.), then $A_2 = A_1 f(x)$ and $B_2 = B_1 f(x)$, so:

$$C_1 = \frac{A_1 B_1 f(x) - A_1 B_1 f(x) + C_2 (A_2 - A_1)}{B_2 - B_1} \quad (4)$$

which may be solved to yield:

$$C_1 = \frac{C_2 A_1 (f(x) - 1)}{B_1 (f(x) - 1)} = C_2 \frac{A_1}{B_1} \quad (5)$$

If R is the measured (observed) ratio at any point, then when sky is present,

$$R = \frac{A+C_1}{B+C_2} \quad (6)$$

then substitution of (5) into (6) yields:

$$R = \frac{A + C_2 \left(\frac{A}{B}\right)}{B + C_2} \quad (7)$$

This reduces to:

$$R = \frac{A(B + C_2)}{B(B + C_2)} = \frac{A}{B} \quad (8)$$

Comparison of (8) with (6) shows that $C_1=C_2=0$, i.e., all sky contamination is removed when the criterion for sky removal is satisfied.

SENSITIVITY CORRECTION

As may be seen in fig. 15, the filter covering the (0-0) band cuts off a small part of that band, while the filter covering the (1-1) band covers that whole band quite well. This difference in relative sensitivity was accounted for by multiplying the (0-0) image by 1.18. Differences in sensitivity for the CCD and the telescope over the small wavelength difference between the two filters were too small to measure, and so no attempt was made to correct for them.

COSMETIC PROCESSING

The high read noise of the Galileo/IfA CCD made it necessary to smooth the data. This smoothing enhanced the visibility of the ratio, particularly near the edges of the images. Thus, all images were smoothed twice, using a routine that averages each pixel's value with that of its neighbors. This has the approximate effect of convolving each image with a two dimensional gaussian with a FWHM of 3 pixels. It was found that smoothing each image 3 times (using a gaussian with a FWHM of ~4 pixels) did not enhance the visibility significantly. The final ratios were sometimes smoothed, as described in the captions of fig. 13.

Some additional "bad" spots remained in the images even after interpolation over the bad columns and removal of the cosmic ray strikes. These were removed interactively, using a routine in which the user specifies the center and radius of the (circular) area to be corrected. The points in the circle are

then replaced by values obtained by cubic spline interpolation of the points in an annulus 3 pixels deep, around the edge of the area. This worked quite well in high signal to noise areas of the images, but gave little improvement in areas near the edges of the images.

CONTINUUM CORRECTION

The processed OH images all had some contribution due to continuum reflection of sunlight off the dust grains in the coma. This was removed by subtracting an image made in a bandpass that had no gaseous emission. This image was aligned with the OH images, scaled, and subtracted.

The image alignment assumed that the optocenters of the gas and dust were at the same point. This assumption is reasonable, given the average guiding errors of ~ 2 arcsec. Telescope drift between exposures precluded any more accurate determination of optocenter offset.

The scaling was determined by comparing profiles through the peaks of the OH images. In this step, the assumption was made that the OH (0-0) band image has virtually no continuum contamination. Spectra of this line (A'Hearn et al. 1983) show that it is about 100 times as strong as the continuum, even at the optocenter (where the continuum is the strongest). In fact, the corrections finally applied had no discernible effect on the appearance of the OH (0-0) image. As mentioned above, it was observed that the continuum images were much more sharply peaked than the OH images. When the OH (1-1) profile was scaled to match the OH (0-0) profile toward the edges, the brightest part of the (1-1) profile (the optocenter) stuck up above the (0-0) profile by a considerable amount (a factor of two in most cases). A fraction of the (aligned) continuum profile was then subtracted from both OH profiles, until the best fit between the (0-0) and (1-1) profiles was obtained (see fig. 11).

Only rarely could the profiles be made to fit exactly. The (1-1) profile often (see Table 4) developed a kink around the central peak, due to over correction, before the central peaks were matched. As discussed in Chapter 3, this residual peak in the OH (1-1) images is believed to be real. It is probably due to the radiative relaxation of OH radicals formed by the dissociation of water molecules. Bertaux (1986) suggested that this dissociation leaves the OH in a highly excited state. The

OH decays from this state primarily by high-level (0-0) transitions, that occur at wavelengths overlapping that the (1-1) band. These higher levels are rarely populated in equilibrium, and thus this excess flux maps out the region in the coma where dissociation of water is primarily taking place. Unfortunately, this region is, in general, small enough that the guiding errors referred to previously preclude any detailed analysis of the destruction of H_2O .

The continuum image was then scaled by the factors determined to give the best match between the OH image profiles, and the result subtracted from the OH images. Errors in the continuum correction were much more obvious in the ratioed images, so several ratios were prepared, with slightly different continuum corrections. The value of the scale factor giving the weakest (none) continuum features in the ratio image was determined. Note that any real gas velocity features that were coincident with continuum features were probably lost in this process. It is unlikely, however, that gas features would follow the continuum features very closely, as gas and dust become decoupled fairly close to the nucleus. An example of this effect is described in Chapter 3. On March 7 there appears a feature of slightly higher ratio in the sunward direction, with a morphology similar to that of some continuum features. The feature in the ratio doesn't match that in the continuum image exactly, however, as it is much less sharply bent, and therefore cannot be completely removed by varying the continuum correction.

The error inherent in this procedure is shown in fig. 14, for a typical night (Jan. 8) and the night with the weakest signal (Oct. 24). The image values are 1σ errors calculated from a simple propagation of errors reduction, considering only errors in the OH band images. The flux in the continuum band was high enough that it did not contribute noticeably to the noise in the ratio. The extinction and continuum correction were determined to about 1%, by the above procedures: their errors can be safely ignored as well.

If A is the flux in a given pixel of the OH (1-1) band, B is the flux in the corresponding pixel in the OH (0-0) band, C similarly for the continuum band image, and a and b are the continuum correction factors for the (1-1) and (0-0) band images respectively, then the ratio R may be written as:

$$R = \frac{A-aC}{B-bC} \quad (9)$$

If σ_0 is the error in a given pixel of the OH (0-0) band image ($\sigma_0 = \text{sqrt}(B)$), σ_1 similarly for the OH (1-1) band image, then the error in the ratio σ_2 may be written:

$$\sigma_2^2 = \sigma_0^2 \left(\frac{A-aC}{(B-bC)^2} \right)^2 + \sigma_1^2 \left(\frac{1}{(B-bC)^2} \right) \quad (10)$$

Figure 14 shows that the error gets larger, farther from the optocenter. This is a direct consequence of the signal strength decreasing away from the optocenter. It is also noticeable that the error is five times greater in October than in January. Even so, ratio values (in October) are good to at least 10% (2% in January). The discrepancy between the observed ratio values and those predicted by Schleicher and A'Hearn is real.

SUMMARY

The general philosophy in preparation of the ratio images was to vary sky and continuum removal, and smooth and "clean up" bad spots on the individual images, until all vestiges of these effects were removed. Once this was accomplished, all remaining features in the ratio image had to be due to the outflow of gas from the nucleus. Unfortunately, a priori methods of sky and continuum removal are not applicable to this data. The images were often obtained at times very different from the standard star measurements, when the sky light was probably much higher (astronomical twilight). Observations of solar-type stars through the filters, when corrected for extinction and compared to give the continuum scale factors (under the assumption that the dust was a neutral reflector), gave obviously erroneous continuum correction factors. Blemishes on the chip are lost data. Interpolation to improve the cosmetic appearance of the images, while justified in this case, is based on the assumption of continuity of the images. At least the determination of the extinction coefficient is fairly straightforward and reliable.

BIBLIOGRAPHY

- A'Hearn, M.F., Feldman, P.D., and Schleicher, D.G.(1983):"The Discovery of S2 in Comet IRAS-Araki-Alcock 1983d", *Ap. J. Lett.* 274, pp. L99-L103
- A'Hearn, M.F., Hoban, S., Birch, P.V., Bowers, C., Martin, R., and Klinglesmith, D.A.(1986):"Cyanogen Jets in Comet Halley", *Nature* 324, pp. 649-651
- A'Hearn, M.F., Hoban, S., Birch, P.V., Bowers, C., Martin, R., and Klinglesmith, D.A.(1987):"Gaseous Jets in P/Halley", *Proc. 20th ESLAB Symp., ESA SP-250, Heidelberg*, vol. 1, pp. 483-486
- Anderson, D.M., and Banin, A.(1974):"Soil and Water and its Relationship to the Origin of Life", in "Origins of Life", vol. 6, pp. 23-26 (Proc. 4th Int'l. Cong. on the Origin of Life, Barcelona, Spain)
- Anderson, D.M.(1967):"Ice Nucleation and the Substrate-Ice Interface", *Nature* 216, pp. 563-566
- Arrhenius, G., and Asunmaa, S.K.(1973):"Aggregation of Grains in Space", *the Moon*, 8, pp. 368-391
- Barshay, S.S., and Lewis, J.S.(1976):"Chemistry of Primitive Solar Material", *Ann. Rev. Astron. Ap.* 14, pp. 81-94
- Bell, J.F., Hawke, B.R., Owensby, P.D., and Gaffey, M.J.(1987):"Atlas of Asteroid Reflection Spectra (0.8-2.5 microns)", pre-print
- Bertaux, J.L.(1986):"The Ultraviolet Bright Spot of Water Vapor in Comets", *Astron. Ap.* 160, pp. L7-L10
- Bradley, J.P., and Brownlee, D.E.(1986):"Cometary Particles: Thin Sectioning and Electron Beam Analysis", *Sci.* 231, pp.1542-1544
- Brin, G.D., and Mendis, D.A.(1979):"Dust Release and Mantle Development in Comets", *Ap. J.* 229, pp. 402-408
- Brownlee, D.E.(1985):"Cosmic Dust:Collection and Research", *Ann. Rev. Earth Plan. Sci.* 13, pp. 147-173
- Campins, H., A'Hearn, M.F., and McFadden, L.-A. (1987):"The Bare Nucleus of Comet Neujmin I", *Ap. J.* 316, pp. 847-857

- Clark, B., Mason, L.W., and Kissel, J.(1987):"Systematics of the "CHON" and Other Light-element Particle Populations in Comet Halley", Proc. 20th ESLAB Symp., ESA SP-250, Heidelberg, vol. 3, pp. 353-358
- Clifford, S.M., and Hillel, D.(1986):"Knudsen Diffusion: The Effects of Small Pore Size and Low Gas Pressure on Gaseous Transport in Soil", Soil Science, 141, pp. 289-297
- Cutts, J.A., and Lewis, B.H.(1982):"Models of the Climate Changes Recorded in Martian Polar Layered Deposits", Ic. 50, pp. 216-244
- Edberg, S.J.(1983):"International Halley Watch Observer's Manual for Scientific Comet Studies, Part II: Ephemeris and Star Charts", JPL Publication 83-16, Pt. 2
- Emerich, C., Lamarre, J.M., Moroz, V.I., Combes, M., Sanko, N.F., Nikolsky, Yu. V., Rocard, F., Gispert, R., coron, N., Bibring, J.P., Encrenaz, T., and Crovisier, J.(1987):"Temperature and Size of Halley's Comet Deduced from IKS Infrared VEGA I Measurements", Proc. 10th ESLAB Symp. on Halleys Comet, vol. II, pp. 381-384
- Fanale, F.P., and Salvail, J.R.(1984):"An Idealized Short-Period Comet Model: Surface Insolation, H₂O Flux, Dust Flux, and Mantle Evolution", Ic. 60, pp. 476-511
- Fanale, F.P., and Salvail, J.R.(1987):"Near Surface Stratigraphy and Thermal Regime of Comet Halley", in preparation
- Festou, M.C.(1981):"The Density Distribution of Neutral Compounds in Cometary Atmospheres I. Model and Equations", Astron. Ap. 95, pp. 69-79
- Gerard, E., Bockelee-Morvan, D., Bourgois, G., Colom, P., and Crovisier, J. (1987):"18 cm Radio Monitoring of the OH Radical in Comet P/Halley 1982i", Proc. 20th ESLAB Symp., ESA SP-250, Heidelberg, vol. 1, pp. 589-594
- German, R.M.(1981):"Porosity and Particle Size Effects on the Gas Flow Characteristics of Porous Metals" Powder Tech. 30,pp. 81-86
- Goldreich, P., and Ward, W.R.(1973):"The Formation of Planetesimals", Ap. J. 183, pp. 1051-1061
- Gradie, J., and Veverka, J.(1980):"The Composition of the Trojan Asteroids", Nature 283, pp. 840-842
- Greeley, R., and Leach, R.(1979):" 'Steam' Injection of Dust on Mars: Laboratory Simulations", NASA TM 80339, pp. 304-307

- Greeley, R.(1979):"Silt-clay Aggregates on Mars", JGR 84, pp. 6248-6254
- Greenberg, R., Weidenschilling, S.J., Chapman, C.R., and Davis, D.R.(1984): "From Icy Planetesimals to Outer Planets and Comets", Ic. 59, pp. 87-113
- Greenberg, J.M.(1982):"What are Comets Made Of? A Model Based on Interstellar Dust", in "Comets", ed. Wilkening, U. Arizona Press, pp. 131-163
- Greenstein, J.L.(1958):"High Resolution Spectra of comet Mrkos (1957d)", Ap. J. 128, pp. 106-113
- Grim, R.E., and Cuthbert, F.L.(1945):"Some Clay-Water Properties of Certain Clay Minerals", J. Am. Ceram. Soc. 28, pp. 90-95
- Grim, R.E.(1968):"Clay Mineralogy", 2nd ed., McGraw-Hill Book Co., N.Y.N.Y.
- Haser, L.(1957): in Bull. Acad. Roy. Sci. Liege 43, p. 740
- Hayatsu, R., and Anders, E.(1981):"Organic Compounds in Meteorites and Their Origins", Topics of Current Chem. 99, pp. 1-37
- Heasley, J.N., Pilcher, C.B., Howell, R.R., and Caldwell, J.(1984):"Restored Methane Band Images of Uranus and Neptune", Ic. 57, pp. 432-442
- Hlivak, R.J., Henry, J.P., and Pilcher, C.B.(1982):"The Galileo/Institute for Astronomy CCD System", Proc. Soc. Photo-Opt. Inst. Eng. 331, pp. 96-103
- Howard, A.D., Cutts, J.A., and Blasius, K.R.(1982):"Stratigraphic Relationships Within the Martian Polar Cap Deposits", Ic. 50, pp. 161-215
- Hsieh, K.C., Curtis, C.C., Fan, C.Y., Hunten, D.M., Ip, W.-H., Keppler, E., Richter, A.K., Umlauf, G., Afonin, V.V., Ero, J., and Somogyi, J.A.(1987): "Anisotropy of the Neutral Gas Distribution of Comet Halley Deduced from NGE/VEGA 1 Measurements", Proc. 20th ESLAB Symp., Heidelberg, ESA SP-250, vol. 1, pp. 417-421
- Johnson, D.W., Harteck, P., and Reeves, R.R.(1975):"Dust Injection into the Martian Atmosphere", Ic. 26, pp. 221-443
- Johnson, R.E., Cooper, J.F., and Lanzerotti, L.J.(1987):"Radiation Formation of a Non-volatile Crust", in Proc. 20th ESLAB Symp., ESA SP-250, Heidelberg, vol. II, pp. 269-272

- Keller, H.U., Arpigny, C., Barbieri, C., Bonnet, R.M., Cazes, S., Coradini, M., Cosmovici, C.B., Delamere, W.A., Huebner, W.F., Hughes, D.W., Jamar, J., Malaise, D., Reitsema, H.J., Schmidt, H.U., Schmidt, W.K.H., Seige, P., Whipple, F. L., and Wilhelm, K.(1986):"First Halley Multicolour Imaging Results from Giotto", Nat. 321, pp. 320-326
- Kissel, J., Sagdeev, R.Z., Bertaux, J.L., Angarov, V.N., Audouze, J., Blamont, J.E., Buchler, K., Evlanov, E.N., Fechtig, H., Fomenkova, M.N., von Hoerner, H., Inogamov, N.A., Khromov, V.N., Knabe, W., Krueger, F.R., Langevin, Y., Leonas, V.B., Lévassieur-Regourd, A.C., Managadze, G.G., Podkolzin, S.N., Shapiro, V.D., Tabaldyev, S.R., and Zubkov, B.V.(1986):"Composition of Comet Halley Dust Particles from VEGA Observations", Nature 321, pp. 280-282
- Kissel, J., Brownlee, D.E., Buchler, K., Clark, B.C., Fechtig, H., Grun, E., Hornung, K., Igenbergs, E.B., Jessberger, E.K., Krueger, F.R., Kuczera, H., McDonnell, J.A.M., Morfill, G.M., Rahe, J., Schwehm, G.H., Sekanina, Z., Utterback, N.G., Volk, H.J., and Zook, H.A.(1986): "Composition of Comet Halley Dust Particles from Giotto Observations", Nature, 321, pp.336-337
- Knacke, R.F., Brooke, T.Y., and Joyce, R.R.(1987):"The 3.2-3.6 μm Emission Features in Comet Halley--Spectral Identifications and Similarities", sub. to Astron and Astroph.
- Krankowsky, D., Lammerzahn, P., Herrwerth, I., Wowries, J., Eberhardt, P., Dolder, U., Herrmann, U., Schulte, W., Berthelier, J.J., Illiano, J.M., Hodges, R.R., and Hoffman, J.H.(1986):"In Situ Gas and Ion Measurements at Comet Halley", Nature 321, pp. 326-329
- Krishna Swamy, K.S.(1986):"Physics of Comets", pub. by World Scientific Publishing Co. Pte. Ltd., Singapore and Philadelphia
- Lane, A.L., Stockton, A.N., and Mies, F.H.(1974):"Ground-based Near Ultraviolet Observations of Comet Kohoutek", in "Comet Kohoutek", NASA SP 355, pp. 87-94
- Larson, H.P., Davis, D.S., Mumma, M.J., and Weaver, H.A.(1986):"Velocity Resolved Observations of Water in Comet Halley", Ap, J. Lett. 309, pp. L95-L99
- Malin, M.C.(1986):"Density of Martian North Polar Layered Deposits: Implications for Composition", GRL 13, pp. 444-447
- McDonnell, J.A.M., Kissel, J., Grun, E., Grard, R.J.L., Langevin, Y., Olearczyk, R.E., Perry, C.H., and Zarniecki, J.C. (1987):"Giotto's Dust Impact Detection system DIDSY and Particle Impact Analyzer PIA: Interim Assessment of the Dust Distribution and Properties within the Coma", Proc. 20th ESLAB Symp. on Halley's Comet, Heidelberg, ESA SP-250, pp. 25-38
- Podolak, M., and Herman, G.(1985):"Numerical Simulations of Cometary Nuclei II: the Effect of the

- Dust Mantle", *Ic.* 61, pp. 267-277
- Pollack, J.B., and Toon, O.B. (1982): "Quasi-Periodic Climate Changes on Mars: A Review", *Ic.* 50, pp. 259-287
- Reitsema, H.J., Delamere, W.A., Keller, H.U., Schmidt, W.K.H., Wilhelm, K., Schmidt, H.U., and Whipple, F.L. (1987): "Nucleus Morphology of Comet Halley", *Proc. 10th ESLAB Conf. on Halley's Comet*, vol. II, pp. 351-354
- Rietmeijer, F.J.M. (1985): "A Model for the diagenesis of Protoplanetary Bodies", *Nature* 313, pp. 293-294
- Samarasinha, N.H., A'Hearn, M.F., Hoban, S., and Klinglesmith, D.A. (1987): "CN Jets in Comet Halley—Rotational Properties", *Proc. 20th ESLAB Symp., ESP SP-250, Heidelberg*, vol. 1, pp. 487-491
- Saunders, R.S., Fanale, F.P., Parker, T.J., Stephens, J.B., and Sutton, S. (1986): "Properties of Filamentary Sublimation Residues from Dispersions of Clays in Ice", *Ic.* 66, pp. 94-104
- Schleicher, D.G., and A'Hearn, M.F. (1982): "OH Fluorescence in Comets: Fluorescence Efficiency of the Ultraviolet bands", *Ap. J.* 258, pp. 864-877
- Simpson, R.A., and Tyler, G.L. (1981): "Viking Bistatic Radar Experiment: Summary of First-Order Results Emphasizing North Polar Data", *Ic.* 46, pp. 361-389
- Singer, R.B. (1985): "Spectroscopic Observations of Mars", *Adv. Sp. Res.* 5, pp. 59-68
- Storrs, A.D., Tokunaga, A.T., Christian, C.A., and Heasley, J.N. (1985): "The Distribution of Dust in the Inner Coma of Comet IRAS-Araki-Alcock (1983d)", *Ic.* 66, pp. 143-153
- Tokunaga, A.T., Nagata, T., and Smith, R.G. (1987): "Detection of a New Emission Band at 2.8 μm in Comet Halley", *sub. to Astron. and Astroph.*
- Weaver, H.A., Mumma, M.J., Larson, H.P., and Davis, D.S. (1986): "Post-Perihelion Observations of Water in comet Halley", *Nature* 324, pp. 441-444